Weak Alfvénic turbulence in relativistic plasmas. Part 2. Current sheets and dissipation

B. Ripperda [1,2,†], **J.F. Mahlmann** [2,†], **A. Chernoglazov** [1,3],
J.M. TenBarge [2,4], **E.R. Most** [5,6,7], **J. Juno** [8], **Y. Yuan** [1],
A.A. Philippov [1] and **A. Bhattacharjee** [2,4]

[1]Center for Computational Astrophysics, Flatiron Institute, 162 Fifth Avenue, New York, NY 10010, USA

[2]Department of Astrophysical Sciences, Peyton Hall, Princeton University, Princeton, NJ 08544, USA

[3]Department of Physics, University of New Hampshire, 9 Library Way, Durham, NH 03824, USA

[4]Princeton Center for Heliophysics, Princeton University, Princeton, NJ 08540, USA

[5]Princeton Center for Theoretical Science, Princeton University, Princeton, NJ 08544, USA

[6]Princeton Gravity Initiative, Princeton University, Princeton, NJ 08544, USA

[7]School of Natural Sciences, Institute for Advanced Study, Princeton, NJ 08540, USA

[8]Department of Physics and Astronomy, University of Iowa, Iowa City, IA 52242, USA

Alfvén waves as excited in black hole accretion disks and neutron star magnetospheres are the building blocks of turbulence in relativistic, magnetized plasmas. A large reservoir of magnetic energy is available in these systems, such that the plasma can be heated significantly even in the weak turbulence regime. We perform high-resolution three-dimensional simulations of counter-propagating Alfvén waves, showing that an $E_{B_\perp}(k_\perp) \propto k_\perp^{-2}$ energy spectrum develops as a result of the weak turbulence cascade in relativistic magnetohydrodynamics and its infinitely magnetized (force-free) limit. The plasma turbulence ubiquitously generates current sheets, which act as locations where magnetic energy dissipates. We show that current sheets form as a natural result of nonlinear interactions between counter-propagating Alfvén waves. These current sheets form owing to the compression of elongated eddies, driven by the shear induced by growing higher-order modes, and undergo a thinning process until they break-up into small-scale turbulent structures. We explore the formation of current sheets both in overlapping waves and in localized wave packet collisions. The relativistic interaction of localized Alfvén waves induces both Alfvén waves and fast waves, and efficiently mediates the conversion and dissipation of electromagnetic energy in astrophysical systems. Plasma energization through reconnection in current sheets emerging during the interaction of Alfvén waves can potentially explain X-ray emission in black hole accretion coronae and neutron star magnetospheres.

Key words: MHD turbulence, turbulence simulation, computational methods, transition to turbulence

† Email addresses for correspondence: bripperda@flatironinstitute.org, mahlmann@princeton.edu

1. Introduction

Plasma turbulence is ubiquitous in the Universe and it is not fully understood how energy cascades to small scales, and how it is eventually dissipated. Turbulent plasma in the magnetospheres of compact objects is typically magnetically dominated, characterized by a magnetization parameter $\sigma = B^2/(4\pi\rho c^2) \geqslant 1$, which indicates that the magnetic energy density $B^2/(4\pi)$ is larger than the rest-mass energy density ρc^2 (Goldreich & Julian 1969; Blandford & Znajek 1977; Duncan & Thompson 1992). The large reservoir of magnetic energy in such relativistic plasmas can be transferred to kinetic and thermal energy through a turbulent cascade. In the relativistic regime, even low-amplitude waves can interact to liberate a significant amount of magnetic energy for dissipation. A variety of astrophysical systems rely on understanding the long-term dynamics of wave interactions, namely how they drive turbulent energy cascades and how energy is eventually dissipated at the smallest scales. Specifically, they are important to understand plasma dynamics in neutron star magnetospheres and X-ray emitting coronae around black hole accretion disks. Magnetars, for example, can emit initially low-amplitude Alfvén waves (AWs) through star quakes that interact with the highly magnetized magnetosphere (Li, Zrake & Beloborodov 2019; Bransgrove, Beloborodov & Levin 2020; Yuan *et al.* 2020*a*). Turbulent black hole accretion disks can emit similar waves, which propagate into their magnetized coronae and can interact with counter-propagating waves (Thompson & Blaes 1998; Chandran, Foucart & Tchekhovskoy 2018). In this work, we explore how overlapping, low-amplitude, Alfvén waves interact in the highly magnetized plasma regime, how they create a weak turbulence spectrum and eventually dissipate. In more realistic magnetospheric settings, Alfvénic fluctuations can be localized in wave packets that travel along a strong guide field (see, e.g. Li *et al.* 2019; Yuan *et al.* 2020*b*). In addition to magnetic energy dissipation arising from the interaction of wave packets, it is crucial to understand the production and dynamics of fast waves (FWs). Unlike Alfvén waves, fast modes are not confined to travel along the strong guide field and are, thus, suitable candidates to transport electromagnetic energy out of the magnetosphere.

We explore the development of weak turbulence through wave interactions in the relativistic, highly magnetized, magnetohydrodynamics (MHD) regime. While MHD is a valid theory for high magnetization, numerically, it is difficult to accurately describe highly magnetized plasma at $\sigma \gtrsim O(10^2)$ (Noble *et al.* 2006; Ripperda *et al.* 2019*a*). Compact object magnetospheres in particular can be so highly magnetized that the infinitely magnetized, or force-free, limit of relativistic MHD[1] is not only applicable (Goldreich & Julian 1969; Blandford & Znajek 1977) but also provides a more accurate numerical method. Although the force-free MHD limit technically cannot describe the physical effects of dissipation, it does capture the formation of a turbulent cascade (Thompson & Blaes 1998; Cho 2005; Li *et al.* 2019) and of current sheets (Mahlmann *et al.* 2021*b*). The force-free MHD limit admits two normal modes, an Alfvén wave and a fast wave. Nonlinear interactions of these waves are expected to result in a turbulent cascade (cf. Takamoto & Lazarian (2017), in the ideal relativistic MHD limit). Wave interactions in the force-free MHD limit have been studied analytically and numerically (Thompson & Blaes 1998; Heyl & Hernquist 1999; Troischt & Thompson 2004; Cho 2005; Li *et al.* 2019), which have emphasized the dominance of either a four-wave interaction of two incoming and two outgoing Alfvén waves as the building blocks of relativistic MHD turbulence (following the Newtonian theory of Sridhar &

---

[1]Note that the Newtonian force-free limit is a subset of the relativistic force-free MHD equations. We refer the reader to the introduction of Mahlmann (2020) for a detailed review of and context for relativistic force-free methods in astrophysics.

Goldreich 1994), or a three-wave interaction of two colliding Alfvén waves producing a fast wave; two fast waves producing a fast wave; and an Alfvén and a fast wave producing an Alfvén wave. Newtonian theory has, however, firmly shown that Alfvén–Alfvén three-wave interactions, which result in an outgoing Alfvén wave, are the dominant building block for MHD turbulence (Montgomery & Matthaeus 1995; Ng & Bhattacharjee 1996; Howes & Nielson 2013; Nielson, Howes & Dorland 2013). TenBarge *et al.* (2021, Paper I of this sequence) concluded both analytically and numerically that the three-wave interaction of two Alfvén waves resulting in a tertiary Alfvén mode is also the fundamental physical process underlying weak relativistic MHD turbulence.

The slope of the turbulent energy spectrum that results from the wave interactions is an open issue that has crucial implications for both plasma turbulence theory as well as plasma dynamics in compact object magnetospheres. In the presence of a uniform magnetic field, the energy spectrum that develops from two interacting Alfvén waves is expected to be anisotropic based on Newtonian MHD weak turbulence theory. In other words, the energy cascade occurs entirely in the direction perpendicular ($\perp$) to the uniform field. In this case, one expects an energy spectrum $E_{B_\perp}(k_\perp) \propto k_\perp^{-2}$ to develop, where $k_\perp$ is the perpendicular Fourier component of the waves (Ng & Bhattacharjee 1997; Galtier *et al.* 2000; Bhattacharjee & Ng 2001; Kuznetsov 2001). In Paper I, we argue that this prediction holds in relativistic MHD turbulence, very much akin to Newtonian theory. In Paper II, we study the shape and formation of a turbulent spectrum arising from the long-term interaction of initially low-amplitude Alfvén waves.

In the Newtonian limit, it has been shown that plasma turbulence intermittently generates small-scale coherent structures in the form of current sheets, which provide the main locations where magnetic energy is dissipated after it cascades (Matthaeus & Lamkin 1986; TenBarge & Howes 2013; Zhdankin *et al.* 2013; Howes 2016; Dong *et al.* 2018; Verniero & Howes 2018; Verniero, Howes & Klein 2018; Rueda *et al.* 2021). These current sheets can be viewed as small-scale eddies stretched along the magnetic field lines, which form as the cascade proceeds towards the smallest dissipative scales (Boldyrev 2006; Loureiro & Boldyrev 2017; Mallet, Schekochihin & Chandran 2017; Comisso *et al.* 2018). Recently, such coherent structures were confirmed to also form in relativistic plasma turbulence (Zhdankin *et al.* 2017; Comisso & Sironi 2018; Nättilä & Beloborodov 2020) and general relativistic, turbulent, black hole accretion flows (Nathanail *et al.* 2020; Ripperda, Bacchini & Philippov 2020). Here, we explore the formation of current sheets as a result of fundamental wave interactions in relativistic, highly magnetized plasma, and their effect on the turbulent spectrum.

This work is organized as a sequence of papers. This manuscript (Paper II) extends the interaction of counter-propagating Alfvén waves (as examined asymptotically in Paper I) up to their turbulent decay in the far nonlinear regime by numerically solving the full three-dimensional (3-D) set of special relativistic ideal MHD equations and their force-free limit. We compare results from independent and different numerical methods to substantiate our findings. The algorithms we employ, the high-order force-free code ET-FFE (Mahlmann *et al.* 2021*a*) and the force-free/relativistic MHD code BHAC (Porth *et al.* 2017; Olivares *et al.* 2019; Ripperda *et al.* 2019*a*), are described in § 2. We explore the nonlinear modelling of continuously overlapping Alfvén waves in detail in § 3, where we provide an analysis of current sheet formation in developing weak turbulence. The formation of current sheets and the dynamics of fast modes as a result of the interaction between localized Alfvén wave packets are examined in § 4. We conclude with a discussion of the obtained results in § 5.

2. Numerical methods

We solve the set of 3-D ideal special-relativistic MHD equations in Cartesian coordinates (x, y, z) using Lorentz–Heaviside units, where a factor of $1/\sqrt{4\pi}$ is absorbed into the electromagnetic fields and velocities are measured in units of the speed of light $c = 1$:

$$\partial_t \boldsymbol{B} + \nabla \times \boldsymbol{E} = 0, \tag{2.1}$$

$$\partial_t D + \nabla \cdot (\rho \Gamma \boldsymbol{v}) = 0, \tag{2.2}$$

$$\partial_t \tau + \nabla \cdot \left(\boldsymbol{E} \times \boldsymbol{B} + \left(h\Gamma^2 - D \right) \boldsymbol{v} \right) = 0, \tag{2.3}$$

$$\partial_t \boldsymbol{S} + \nabla \cdot \left(-\boldsymbol{E}\boldsymbol{E} - \boldsymbol{B}\boldsymbol{B} + h\Gamma^2 \boldsymbol{v}\boldsymbol{v} + \left[\tfrac{1}{2} \left(E^2 + B^2 \right) + p \right] \right) = 0. \tag{2.4}$$

In the ideal MHD limit, the electric field is not evolved, but given by the relation $\boldsymbol{E} = -\boldsymbol{v} \times \boldsymbol{B}$, dependent on the velocity field $\boldsymbol{v}$ and the magnetic field $\boldsymbol{B}$. The conserved mass density D, energy density τ and energy flux density $\boldsymbol{S}$ are given by

$$D = \Gamma \rho, \tag{2.5}$$

$$\tau = \tfrac{1}{2}(E^2 + B^2) + h\Gamma^2 - p - D, \tag{2.6}$$

$$\boldsymbol{S} = \boldsymbol{E} \times \boldsymbol{B} + h\Gamma^2 \boldsymbol{v}, \tag{2.7}$$

where the enthalpy $h = \rho(1 + \varepsilon) + p$ is given in terms of the rest-mass density ρ and specific internal energy ε. In the following, we adopt the ideal fluid equation of state, $p = \rho\varepsilon(\hat{\gamma} - 1)$, with an adiabatic index $\hat{\gamma} = 4/3$. We find it useful to define the dimensionless magnetization parameter as the ratio between magnetic enthalpy density and rest-mass density with $\sigma = B^2/\rho$. We note that $\sigma_{\text{hot}} = B^2/h$ is commonly used to specify the magnetization of hot plasma as it accounts for non-vanishing thermal pressure; it defines the Alfvén speed $v_A = \sqrt{\sigma_{\text{hot}}/(1 + \sigma_{\text{hot}})}$. The gas to magnetic pressure ratio $\beta = 2p/B^2$ is limited to $\beta \leqslant 1/(2\sigma_{\text{hot}})$. The fluid velocity $\boldsymbol{v}$ measured by an inertial observer has the corresponding Lorentz factor $\Gamma = (1 - v^2)^{-1/2}$. We note that an observer locally comoving with velocity $\boldsymbol{v}$ will measure the magnetic energy density $b^2 = B^2/\Gamma^2 + (\boldsymbol{B} \cdot \boldsymbol{v})^2$.

In addition, we will also consider the limit of negligible plasma inertia and pressure, namely $\sigma \to \infty$ and, hence, $v_A \to 1$. This limit corresponds to a vanishing Lorentz force, $q\boldsymbol{E} + \boldsymbol{J} \times \boldsymbol{B} = 0$, which implies that $\boldsymbol{E} \cdot \boldsymbol{B} = 0$ and also requires magnetic dominance $E^2 < B^2$. Here, $q = \nabla \cdot \boldsymbol{E}$ is the charge density and $\boldsymbol{J}$ is the current as seen by an inertial observer. We treat this limit by solving the following set of special-relativistic force-free MHD equations (e.g. Gruzinov 1999; Blandford 2002):

$$\partial_t \boldsymbol{B} + \nabla \times \boldsymbol{E} = 0, \tag{2.8}$$

$$\partial_t \boldsymbol{E} - \nabla \times \boldsymbol{B} = -\boldsymbol{J}, \tag{2.9}$$

with force-free current density

$$\boldsymbol{J} = q\frac{\boldsymbol{E} \times \boldsymbol{B}}{B^2} + \frac{\boldsymbol{B} \cdot (\nabla \times \boldsymbol{B}) - \boldsymbol{E} \cdot (\nabla \times \boldsymbol{E})}{B^2}\boldsymbol{B}. \tag{2.10}$$

The force-free limit of MHD does not describe the physics of dissipative mechanisms like magnetic reconnection. Dissipation is instead the result of the numerical procedure applied to obey the ideal force-free conditions $\boldsymbol{E} \cdot \boldsymbol{B} = 0$ and $E^2 < B^2$. Enforcing these

conditions, particularly in reconnecting current sheets, i.e. where the reconnecting components of the magnetic field go to zero, results in the removal of electromagnetic energy from the system. We perform our force-free MHD simulations with two different and independent algorithms (BHAC and ET-FFE, described below) that enforce the ideal force-free conditions in different manners. We compare the results to assure that the turbulent cascade, the formation process of current sheets in weak turbulence conditions and the thinning of those current sheets are accurately captured. We also test the robustness and convergence of our force-free MHD results for a large number of characteristic timescales by simulating the same set-up for increasing resolutions. Finally, the relativistic ideal MHD capacities of BHAC allow us to extend our results to finite magnetizations as opposed to the force-free limit. We outline the details of the numerical algorithms below.

Mahlmann *et al.* (2021*a*) introduced a scheme based on the infrastructure of the EINSTEIN TOOLKIT,[2] here dubbed ET-FFE, specifically designed for the high-order conservative modelling of the force-free electrodynamics equations (2.8)–(2.9). The charge density is evolved in a separate continuity equation and the algorithm relies on the fully consistent force-free current (2.10). Hyperbolic/parabolic cleaning is used to maintain a solenoidal magnetic field and a conserved electric charge. Algebraic corrections are applied when numerical violations of the force-free constraints occur. The combination of algebraic corrections and the consistent ideal force-free current does not require implicit steps in the time integrator. Therefore, employing MP7 (Suresh & Huynh 1997) spatial reconstruction and fourth-order accurate time integration results in very competitive convergence of the numerical diffusion and dispersion (Mahlmann *et al.* 2021*b*). These properties are essential for the robustness of the results presented in this manuscript.

BHAC (Porth *et al.* 2017; Olivares *et al.* 2019) can capture the transformation of electromagnetic to kinetic and thermal energy when performing simulations for finite magnetization by evolving the full set of ideal special-relativistic MHD equations (2.1)–(2.4). Additionally, the set of force-free MHD equations (2.8)–(2.9) is implemented in the relativistic resistive MHD framework in BHAC (Ripperda *et al.* 2019*a*,*b*), in combination with the resistive force-free Ohm's law of Alic *et al.* (2012) replacing (2.10),

$$
J = q\frac{E \times B}{B^2} + \frac{1}{\eta}\left[(E \cdot B)\frac{B}{B^2} + \Theta(E^2 - B^2)\frac{E}{B^2}\right], \tag{2.11}
$$

which imposes the force-free conditions using a damping current on timescales set by an effective resistivity η, which is smaller than the time step Δt of our simulation. We employ a fiducial, small, uniform and constant resistivity $\eta = 10^{-6}$, and show that larger values have a significant effect on the large-scale damping of the total electromagnetic energy owing to Ohmic heating. The second damping term (proportional to $E^2 - B^2$ in (2.11)) only needs to be activated locally when $E^2 > B^2$, which rarely occurs in weak turbulence with a strong guide field, and we therefore make use of the Heaviside function Θ. Throughout this manuscript, BHAC is used for both relativistic ideal MHD simulations with different magnetizations and force-free MHD simulations. To treat small damping timescales and, hence, stiff source terms in the electric current, we use an implicit–explicit (IMEX) Runge–Kutta time integrator (Pareschi & Russo 2005). We compute curl and divergence terms in the evolution equations using a second-order accurate finite-volume scheme composed of a Rusanov Riemann solver (Rusanov 1961) paired with a third-order accurate monotonicity preserving reconstruction scheme (Čada & Torrilhon 2009). The solenoidal magnetic field constraint, $\nabla \cdot B = 0$, is enforced to machine precision by means

[2]http://www.einsteintoolkit.org

of a staggered constrained transport scheme (Evans & Hawley 1988; Olivares *et al.* 2019), where the electric fluxes are computed using the upwind-constrained transport scheme (Londrillo & del Zanna 2004). Instead of evolving the charge density q, it is obtained by numerically taking the divergence of the evolved electric field as $q = \nabla \cdot \boldsymbol{E}$ at every time step of the simulation. While this may lead to a small non-conservation of global charge, we have found the effect to be negligible (Ripperda *et al.* 2019a). The implementation of the IMEX scheme used for the solution of the force-free MHD equations is presented by Ripperda *et al.* (2019a,b) in the context of resistive relativistic MHD.

Our results are numerically converged between the two force-free MHD algorithms at the high resolutions we employ, and in Appendix A, we show that dispersion and diffusion errors never dominate on the evolved timescales. The high-order reconstruction capacities of ET-FFE compensate for the significant factor of resolution needed in lower-order methods, such as BHAC. We present results that converge between two different implementations of the force-free limit of MHD. Different techniques to process violations of the force-free conditions can alter the global field dynamics. Comparing two methods that use the two most commonly employed correction methods (namely, algebraic resets and charge conservation in ET-FFE versus driving currents in BHAC with a finite resistivity η) supports the reliability and reproducibility we claim for our results. In Appendix B, we show that the formation of current sheets in weak turbulence with a strong guide field is captured by both force-free MHD algorithms and that ideal force-free violations are negligible until the current sheets break-up.

3. Overlapping Alfvén waves

Interacting Alfvén waves, for example launched into the magnetosphere of a compact object, can result in the development of a weak turbulence cascade (Chandran *et al.* 2018; Yuan *et al.* 2020a). In this section, we set up a toy problem of two overlapping perpendicularly polarized counter-propagating Alfvén waves. The waves are initialized on top of each other and cover the entire 3-D domain with periodic boundaries. This initial condition reproduces all the characteristics of the nonlinear interactions described theoretically in Paper I. We explore the development of a weak turbulence spectrum and the formation of current sheets owing to the interaction of the waves, which can provide a viable dissipation route.

3.1. *Wave initialization*

We consider the nonlinear interaction between two overlapping, perpendicularly polarized Alfvén waves that counter-propagate in a periodic 3-D domain along a uniform guide field $\boldsymbol{B_0} = B_0\hat{\boldsymbol{z}}$. The waves are described by positive constants representing the components of the wave vector that are perpendicular ($k_\perp$) and parallel ($k_\parallel$) to the guide field $\boldsymbol{B_0}$. We employ a cubic box with $L_\perp = L_x = L_y = 2\pi$, $L_\parallel = L_z = 2\pi$ and a uniform resolution of $(N_x, N_y, N_z) = (N_\perp, N_\perp, N_\parallel)$ cells per initial wavelength. For a scale-free definition of characteristic (wave)lengths, we prescribe $k_\parallel = 2\pi/L_\parallel$ and $k_\perp = 2\pi/L_\perp$. Then, we examine the waves described by the wave vectors $\boldsymbol{k_1^+} = k_\perp\hat{\boldsymbol{x}} - k_\parallel\hat{\boldsymbol{z}}$, from now on represented as $(1, 0, -1)$ and $\boldsymbol{k_2^-} = k_\perp\hat{\boldsymbol{y}} + k_\parallel\hat{\boldsymbol{z}}$, or $(0, 1, 1)$. The magnetic field is initialized through a vector potential $\boldsymbol{A} = (-B_0y, 0, \delta B_\perp[\sin(k_\perp x + k_\parallel z) + \sin(k_\perp y - k_\parallel z)])$, which represents the initial counter-propagating Alfvén waves with frequency $\omega_0 = k_\parallel v_A$ and $\hat{B} = \delta B_\perp/B_0$. The electric field is initialized as $\boldsymbol{E} = (v_A B_y, v_A B_x, 0)$ such that the velocity is equal to the drift velocity $\boldsymbol{v} = \boldsymbol{E} \times \boldsymbol{B}/B^2$. We note that the overlapping Alfvén waves, in contrast to a single Alfvén wave, are not an exact force-free MHD equilibrium owing to a small second-order violation $\boldsymbol{E_\mp} \cdot \boldsymbol{B_\pm} \neq 0$ between the fields of the two waves.

These perturbations are instantaneously algebraically cut in ET-FFE and damped on a short timescale in BHAC. Initially, we set a gas to magnetic pressure ratio of $\beta = 2p/B_0^2 = 0.02$ and set the magnetization $\sigma \in [10^{-2}; 10^{-1}; 1; 10; 100]$ (corresponding to $\sigma_{hot} \in [10^{-2}; 10^{-1}; 1; 7; 20]$), where we vary the density ρ and keep a constant guide field with $B_0 = 1$. We fix the pressure to $p = 0.01$ and employ an adiabatic index $\hat{\gamma} = 4/3$ for an ideal relativistic gas. In the force-free MHD case, $\beta \to 0$, $\sigma \to \infty$ and $v_A \to 1$.

Through the three-wave interaction, turbulence can transfer magnetic energy anisotropically from large to small scales. The two initial waves interact to form an inherently nonlinear, purely magnetic mode, physically representing a shear in the magnetic field with wave vector $\mathbf{k}_2^0 = k_\perp(\hat{\mathbf{x}} + \hat{\mathbf{y}})$, or $(1, 1, 0)$, which does not grow secularly in time but oscillates at twice the frequency of the primary waves (see Paper I). The interaction between this secondary mode and the primary Alfvén modes nonlinearly generates two tertiary Alfvén waves whose energy grows secularly in time. The $\mathbf{k}_1^+$ wave transfers energy to an Alfvén mode with $\mathbf{k}_3^+ = 2k_\perp\hat{\mathbf{x}} + k_\perp\hat{\mathbf{y}} - k_\parallel\hat{\mathbf{z}}$, or $(2, 1, -1)$, and the $\mathbf{k}_1^-$ wave to $\mathbf{k}_3^- = k_\perp\hat{\mathbf{x}} + 2k_\perp\hat{\mathbf{y}} + k_\parallel\hat{\mathbf{z}}$, or $(1, 2, 1)$.

To capture all physical behaviour including nonlinear interactions at play in magnetized turbulence, we solve the full 3-D set of equations. The strength of the nonlinearity is characterized by $\chi = k_\perp v_\perp/(k_\parallel v_A)$, where $k_\perp = k_\parallel$ in the set-up presented in this section, and $v_\perp/v_A \sim \delta B_\perp/B_0 = 10^{-1}$. This gives $\chi = 10^{-1}$, which results in a nonlinear time of $\chi^{-2} = 100$ wave-crossings $2\pi/\omega_0$. The limit of strong turbulence occurs when the nonlinear energy transfer timescale is comparable to the wave period, as to say, when $\chi \gtrsim 1$ (Goldreich & Sridhar 1995). The nonlinearities governing these dominant three-wave interactions require variations in both directions perpendicular to the equilibrium magnetic field (Howes & Nielson 2013; Howes 2014, Paper I). In the two-dimensional (2-D) limit perpendicular to the uniform field, the dominant nonlinearities governing the three-wave interactions are retained, yet the linear physics of the anisotropic cascade is absent: the linear interactions representing the propagation of the Alfvén waves along the magnetic field are only non-zero when the parallel wavenumber $k_\parallel$ is non-zero, which requires a (third) field-parallel dimension.

3.2. *Current sheet formation*

In this section, we analyse the formation of the sheets, their thickness, and the dynamics until the moment they break-up and magnetic energy is quickly dissipated. As shown in Paper I, the energy transfer to smaller scales is mediated by self-consistently generated $k_\parallel = 0$ modes in the $\chi \ll 1$ limit, specifically, at least until the nonlinear time of $\sim \chi^{-2} = 100$ wave-crossings. If the nonlinearly generated Alfvén waves increase in power, they can generate coherent current sheet-like structures owing to constructive interference with the primary Alfvén modes. Although in the ideal limit, current sheets are Dirac delta-functions, at finite dissipation, they can be represented by many fewer modes such as those in Howes (2016), who showed that the formation of current sheets results from interference between just five complex Fourier modes. To study whether current sheets can form and become thin enough to provide an efficient dissipation channel, we evolve the system for 200 wave-crossings, beyond the nonlinear time of $\sim \chi^{-2} = 100$ wave-crossings.

Current sheets emerge once the wave interaction reaches a nonlinear state. To track the dynamics of an emerging current sheet, we show the evolution of the normalized in-plane current density $\hat{J}_z = [\nabla \times \mathbf{B}]_z/(k_\parallel B_0)$[3] perpendicular to the equilibrium field

---

[3]We confirmed that the contribution of the displacement current $d\mathbf{E}/dt$ to the current density is negligible and $\mathbf{J} \approx \nabla \times \mathbf{B}$.
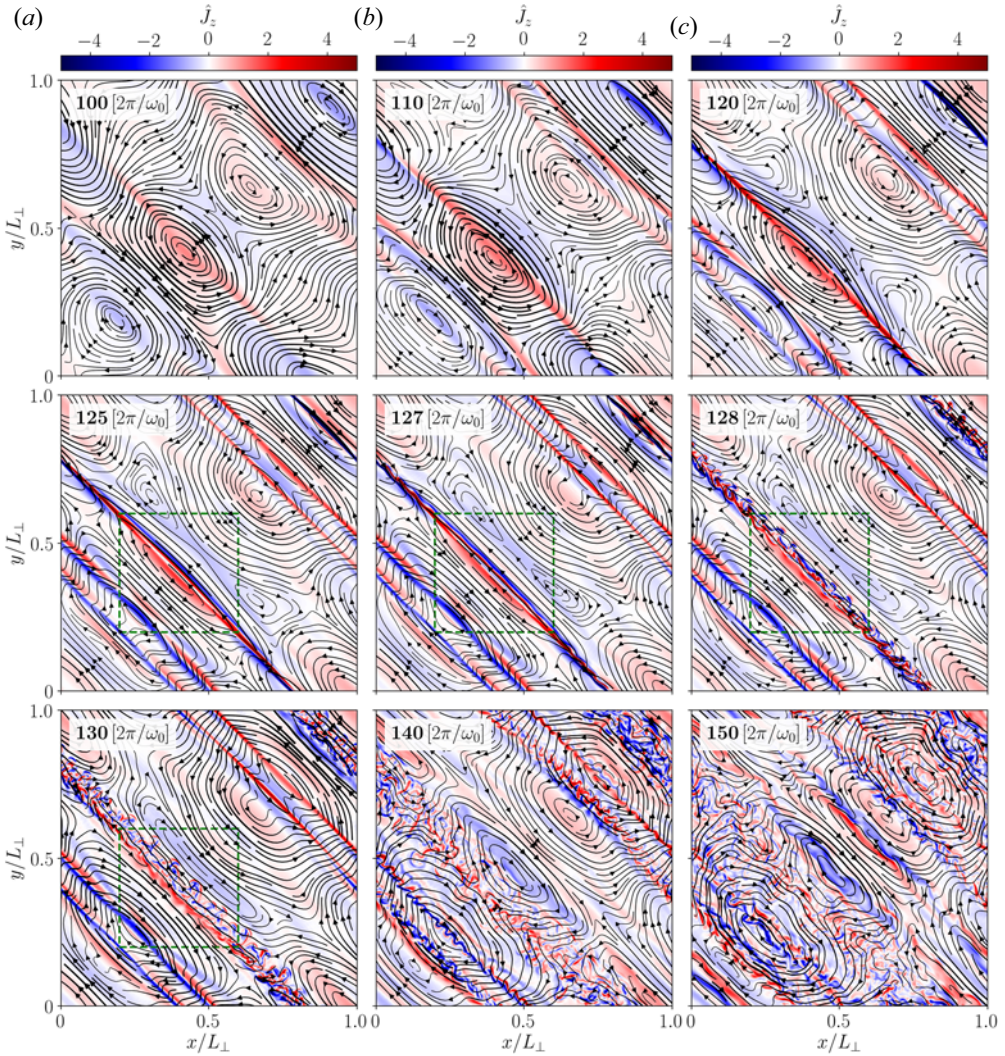
FIGURE 1. Normalized out-of-plane current density $\hat{J}_z = [\nabla \times \boldsymbol{B}]_z/(k_\perp B_0)$ in the (x, y)-plane perpendicular to the guide field showing the formation ($t \lesssim 100\,[2\pi/\omega_0]$), thinning ($t \sim 100 - 120\,[2\pi/\omega_0]$) and break-up of current sheets ($t \sim 120$–$130\,[2\pi/\omega_0]$) into developed turbulence ($t \gtrsim 130$–$150\,[2\pi/\omega_0]$) with ET-FFE. In-plane magnetic field lines are overplotted. We note that the evolution of the current density is similar for a run at 1024^3 cells with BHAC. Figure 4 presents a 3-D rendering of the evolving current sheet enclosed by the dashed green rectangles. An animated version of this figure is provided in Media Supplement A (2021).

$\boldsymbol{B} = B_0\hat{z}$ at $z = \pi$ between 100 and 150 wave-crossings in figure 1, for the ET-FFE run with 512^3 grid-points. We find that the results from ET-FFE (512^3) are comparable to the high-resolution runs conducted with BHAC (1024^3). The high-order reconstruction methods employed in ET-FFE capture the smallest scales with very good accuracy (see also § 3.3 and Mahlmann *et al.* 2021b). Current sheets are characterized by in-plane magnetic field line reversals (overplotted as black lines) and are clearly distinguishable by a strong current density (red and blue colours). At the interface of interacting eddies, current sheets are compressed into thin layers, as we examine in detail in figure 2. In
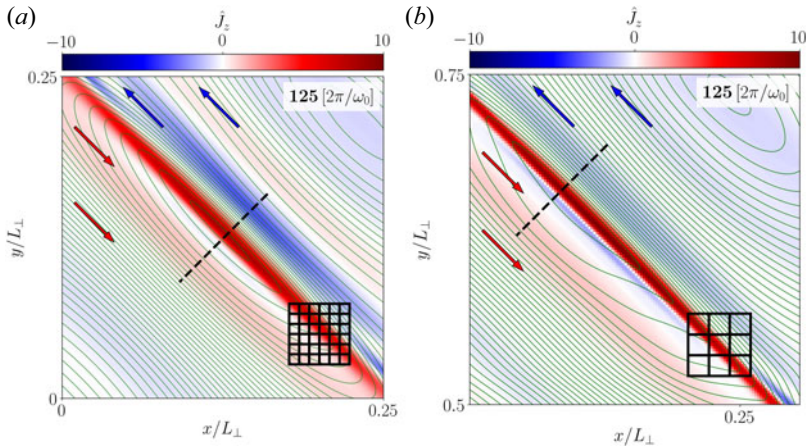
FIGURE 2. Current sheets form between elongated eddies. Zoomed-in view of the out-of-plane current density $\hat{J}_z = [\nabla \times \boldsymbol{B}]_z/(k_\perp B_0)$ at 125 wave-crossings. Contours of the out-of-plane vector potential A_z (where $\boldsymbol{B} = \nabla \times \boldsymbol{A}$), which represent in-plane magnetic field lines, are overplotted in green, showing that regions of large current density originate from compressed magnetic field (direction indicated by arrows). We select the strongest current sheet in the domain of a BHAC 1024^3 simulation (*a*) and an ET-FFE 512^3 set-up (*b*). To indicate the respective applied resolutions, we show a fraction of the numerical grid stacked with blocks, where each block consists of 8×8 cells. The current sheets (in bright red) are covered along their thickness $\delta \approx 0.01 \times 2\pi \approx 0.06$ by at least 8 cells in both cases. A one-dimensional (1-D) outline of field quantities across the centre of each current sheet (dashed black lines) is presented in figure 3.

figure 1, such regions are indicated by an anti-parallel in-plane magnetic field, for example at $x = 0.9\pi$, $y = 0.9\pi$ at $t = 125\ [2\pi/\omega_0]$. We also detect regions of non-zero current density which are not associated with current sheets owing to the lack of anti-parallel magnetic field, i.e. there is no in-plane magnetic null, as in figure 1 at $x = 0.7\pi$, $y = 0.7\pi$ at $t = 110\ [2\pi/\omega_0]$.

The current sheets in this system can be characterized by the aspect ratio in the perpendicular plane between their thickness, δ, and width, w. We determine δ as the full-width at half maximum of the out-of-plane current density $\hat{J}_z$. The sheet becomes thinner between 100 and 127 crossings, until it breaks up. The width of the sheet w, namely, its extension along the interface of two eddies, is determined by the perpendicular wavelength $\lambda_\perp = 2\pi$ of the initial waves in the box. It remains approximately constant $w \approx 2\pi$ from its formation at 100 crossings until the sheet breaks up at 127 crossings (see also figure 3). The aspect ratio decreases from $\delta/w \gtrsim 0.025$ (ET-FFE) at 100 wave-crossings onward to $\delta/w \approx 0.01$ (ET-FFE/BHAC) at 125 wave-crossings (see also figure 3(*e*), indicated by the black dashed line). The reconnection rate is expected to scale with the aspect ratio, $v_{\text{rec}}/c \sim \delta/w$, which suggests that the sheet breaks up in the linear regime of the instability (Biskamp 2000; Ni *et al.* 2010), and in the nonlinear regime, the asymptotic 'fast reconnection rate' (Bhattacharjee *et al.* 2009; Uzdensky, Loureiro & Schekochihin 2010; Huang & Bhattacharjee 2016) of 0.01 might be reached. The life-time of the sheets is approximately 25 wave-crossings, and hence it is maintained on timescales (and length scales) of the initial large-scale waves (cf. Howes, McCubbin & Klein 2018). Turbulent fluctuations initiate inside the current sheets after 125 wave-crossings, where energy is quickly dissipated at the grid scale, which is smaller than the current sheet thickness, $\Delta x/\delta \lesssim 0.2$.
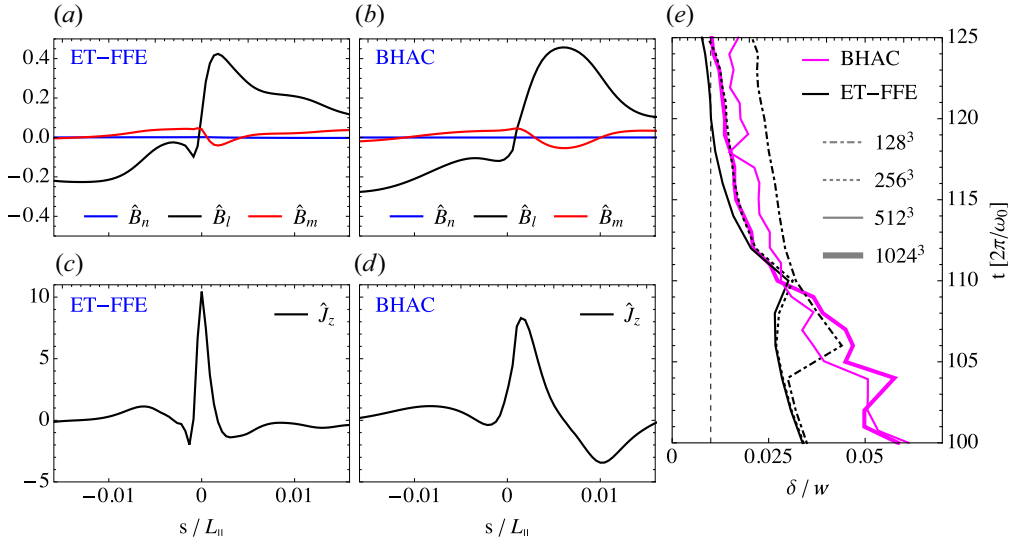
FIGURE 3. Current sheets form similarly across different codes and resolutions. Profiles of normalized magnetic field $\hat{B}_i = \delta B_i / B_0$ (*a,b*) in minimum variance coordinates (cf. Sonnerup & Cahill 1967; Howes 2016), and out-of-plane current density $\hat{J}_z = [\nabla \times B]_z / (k_\perp B_0)$ (*c,d*) at $t = 125\ [2\pi/\omega_0]$. The 1-D outlines are extracted across the current sheet (see dashed black lines in figure 2), where the coordinate s is centred at the respective structure. (*e*) Aspect ratio δ/w of the current sheet measured as the full-width half maximum of the current density normalized by its approximately constant width $w \approx 2\pi$ versus wave-crossings for both BHAC and ET-FFE. The current sheet forms around the nonlinear time $t = 100\ [2\pi/\omega_0]$ and the thinning process halts at around 125 wave-crossings at $\delta/w \approx 0.01$, which suggests that the sheet breaks up once an asymptotic reconnection rate $v_{rec}/c \sim \delta/w \approx 0.01$ (indicated by a vertical dashed line) is reached.

The 3-D structure of the current sheet is lucidly illustrated in figure 4. We provide a volume rendering of $\hat{J}_z$ and observe a clear coherent structure that breaks after 127 wave-crossings. Initially, the current structure is, indeed, sheet-like in three dimensions. In the direction parallel to the guide field, the characteristic scale is the current sheet's length, L. We measure the length of the sheet along the z-axis to be $L \approx 2\pi$, which is determined by the parallel wavelength $\lambda_\parallel = 2\pi$ along the equilibrium magnetic field. At the same time, it becomes visually evident that the extension in the plane perpendicular to the guide field is less than the box diagonal, but rather corresponds to $w \approx 2\pi$ (see above). At $t = 125\ [2\pi/\omega_0]$, the current sheet is already very thin (see also figure 1). In the very short time interval of $\Delta T \approx 5\ [2\pi/\omega_0]$, the current sheet ripples and breaks up into turbulent structures in the plane perpendicular to the guide field. During this time, we identified that non-ideal electric fields build up in the localized region of the current sheet. Such fields are subsequently damped to maintain a (globally) force-free field configuration.

3.3. *Comparison of current sheet characteristics in ET-FFE and BHAC*

The emerging current sheet is analysed in detail in figures 2 and 3 and compared between the employed numerical schemes. We illustrate the current sheet properties and their numerical resolution in figure 2. There, we plot numerical blocks of 8×8 cells in a zoom-in on the strongest currents in the domain, which shows that the current sheet is indeed resolved by more than one block (approximately 11 cells) at the break-up time when the sheet is at its thinnest point, in the case of BHAC with a total of 1024^3 cells,
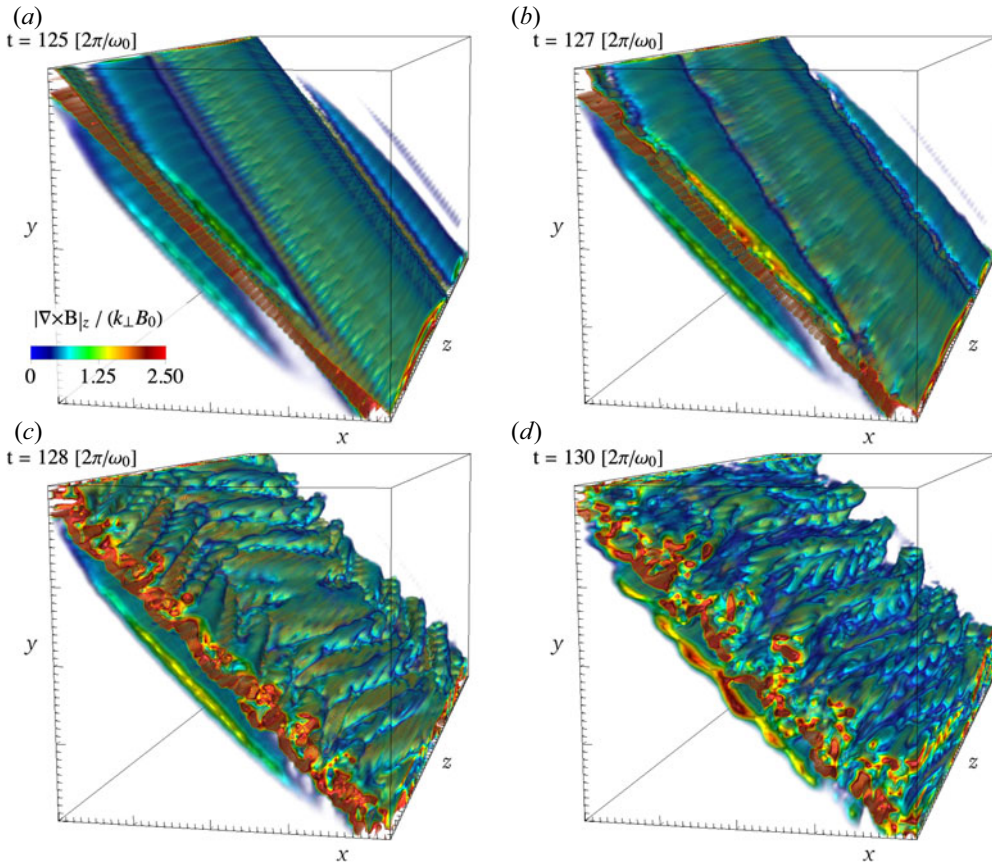
FIGURE 4. Volume rendering of the normalized out-of-plane current density $\hat{J}_z = [\nabla \times \boldsymbol{B}]_z/(k_\perp B_0)$, which shows the moment of the break-up of the current sheet between $t = 125\ [2\pi/\omega_0]$ and $t = 130\ [2\pi/\omega_0]$, within the reduced volume $x \times y \times z = [2\pi/5, 6\pi/5] \times [2\pi/5, 6\pi/5] \times [0, 2\pi]$ at a resolution of 512^3. An animated version of this figure is provided in Media Supplement B (2021).

and by slightly less than one block (approximately 8 cells) in the case of ET-FFE with a total of 512^3 cells. While such resolution arguments do not imply a convergence of dissipative dynamics in the force-free current sheet, they correspond to the minimum resolution needed to capture their formation in the magnetically dominated regime (as was established by Mahlmann *et al.* 2021*b*, namely, 5 to 10 cells per current sheet width). A notable characteristic of the examined sheet can be drawn from the overplotted contours of the out-of-plane vector potential A_z (green lines): one can see that the regions of high current density originate from magnetic field compression at the edges of the elongated eddies.

The current sheet formation and evolution are very similar for the different codes and resolutions. In figure 3(*a*,*b*), we show the normalized magnetic field $\hat{B}_i = \delta B_i/B_0$ and (*c*,*d*) show the normalized out-of-plane current density $\hat{J}_z = [\nabla \times \boldsymbol{B}]_z/(k_\parallel B_0)$ along a cut perpendicular to the current sheet presented in figure 2 just before it breaks at the time $t = 125\ [2\pi/\omega_0]$. In this analysis, we choose minimum variance coordinates (cf. Sonnerup & Cahill 1967; Howes 2016) for comparability. These coordinates combine the guide field direction $\hat{\boldsymbol{m}} = \hat{\boldsymbol{z}}$, as well as the in-plane directions $\hat{\boldsymbol{n}} = (\hat{\boldsymbol{x}} + \hat{\boldsymbol{y}})/\sqrt{2}$ and

$\hat{l} = (\hat{x} - \hat{y})/\sqrt{2}$. For both BHAC and ET-FFE, we use the location of the strongest current in the domain for the analysis (indicated by the black dashed line in figure 2). The current sheet shows a typical profile with a peak in the current density and magnetic field reversals of the reconnecting in-plane components $\hat{B}_x$ and $\hat{B}_y$ (i.e. the perpendicular component $\hat{B}_l$). The gradient of the guide field pressure (red line) is non-zero in the current sheet, which compensates for gas pressure that is absent in the force-free limit of MHD, and effectively working to sustain the evolving force-free current sheet by a locally balanced magnetic pressure at the location of the field reversal (similar to the stationary force-free current sheets analysed by Komissarov, Barkov & Lyutikov 2007; Del Zanna *et al.* 2016; Mahlmann *et al.* 2021*b*).

The process of current sheet formation and thinning is independent of the manner in which force-free violations are managed (see also Appendix B) and is likely dominated by the field compression driven by mode interactions. The thickness $\delta = 0.01w$ after 125 crossings is approximately 10 times larger than the smallest resolvable perpendicular scale in the BHAC simulation, $\sim 2\pi/1024$ and five times larger than the smallest resolvable scale in the ET-FFE simulation, $\sim 2\pi/512$ (figure 3*e*). Additionally, we measure the thickness of the current sheet in time for progressively increasing resolutions in the right panel, which shows that the thinning rate and aspect ratio in ET-FFE converges for 256^3 and 512^3 grid points, while for BHAC, it converges for 512^3 and 1024^3 grid points. The thinning rate and aspect ratio also converge between the highest resolution results of the two different algorithms. We demonstrate that the current sheet's thickness is larger than a single numerical cell by measuring the number of cells across the sheet's thickness at 125 wave-crossings just before the sheet breaks up. The observation that the current sheet formation, thinning as well as asymptotic thickness and time of break-up coincide between runs in BHAC and ET-FFE (with a largely different order of convergence and treatment of the force-free violations) is worth mentioning in this context. Small local differences aside, the comparison of results from the two numerical schemes in figures 2 and 3 shows that the field structure is remarkably similar in both cases. The global dynamics of field compressions is captured accurately in the force-free limit of MHD. In Appendix B, we compare the appearance of non-ideal electric fields in both methods, and conclude that despite numerical differences, the results show a remarkable level of similarity both in magnitude and location of the force-free violations.

In summary, the following features let us conclude that the identified structures are 3-D current sheets: (*a*) strong and localized ordered current structures; (*b*) field reversals with a compensating magnetic pressure; (*c*) compression and subsequent thinning of the current structure; and (*d*) non-ideal electric fields around magnetic null-lines (see Appendix B) in the plane perpendicular to the guide field.

3.4. *Weak turbulence development*

In this section, we investigate how energy cascades and dissipates at small scales. In force-free MHD, the total electromagnetic energy is conserved in the domain until the turbulent cascade reaches the numerical grid scale. By measuring the total electromagnetic wave-energy $E_{\mathrm{EM}} = (B - B_0)^2 + E^2$, we determine the dissipation rate depending on the resolution and the explicit resistivity, η (in BHAC runs). For a resolved simulation, i.e. where the current sheet thickness is resolved by multiple cells, the energy E_{EM} should dissipate as $\mathrm{d}E_{\mathrm{EM}}/\mathrm{d}t \sim \boldsymbol{E} \cdot \boldsymbol{J} \sim \eta J^2 \sim \eta|\nabla \times \boldsymbol{B}|^2$, where $\nabla \times \boldsymbol{B} \sim B_k/\lambda$ and $\lambda = 2\pi$ is the wavelength, which implies that the typical dissipation time is $\tau \sim \lambda^2\eta^{-1}$, such that we can approximate the total energy as $E_{\mathrm{EM}}(t) \approx E_{\mathrm{EM},t=0}(1 - \eta(2\pi t/\omega_0))$. Figure 5(*a*) shows
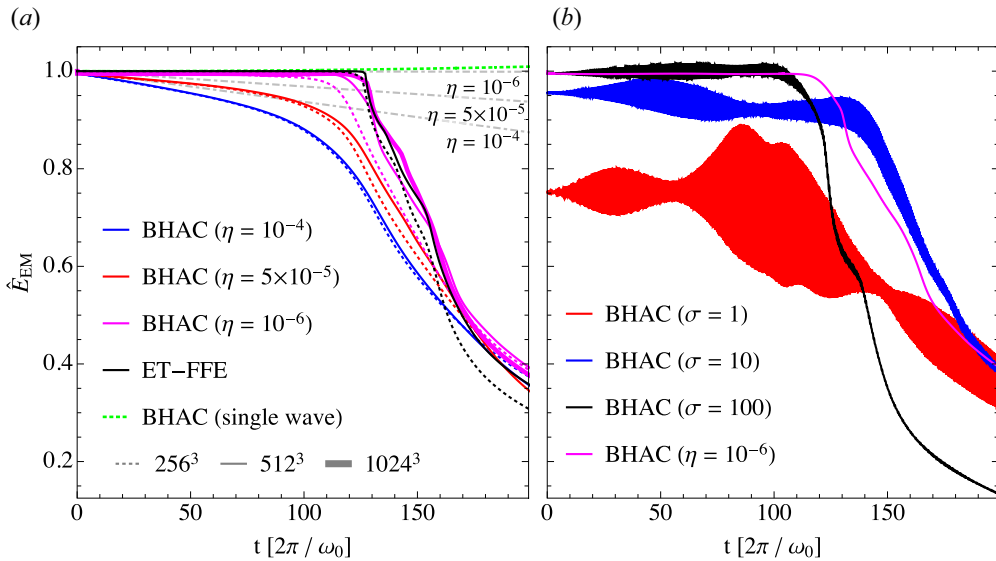
FIGURE 5. Evolution of the (normalized) total wave energy $\hat{E}_{\mathrm{EM}} = E_{\mathrm{EM}}/E_{\mathrm{EM},t=0}$, with $E_{\mathrm{EM}} = (B - B_0)^2 + E^2$ for the overlapping Alfvén waves in all force-free MHD cases at different resolutions (*a*). We present ideal MHD cases and a force-free reference case ((*b*), BHAC) normalized to the initial electromagnetic wave energy of the force-free set-up for 200 wave-crossings, with initial wave-amplitude $\chi = 10^{-1}$ and $N_\perp = N_\parallel = 512$ grid-cells. In (*a*), we overplot results for BHAC (blue, red and magenta lines for different resistivities; dotted, solid and thick lines for different resolutions) at resolutions $N_\perp = N_\parallel = 256$, 512 and 1024 as well as ET-FFE (black lines) at 256 and 512 grid cells to show that the energy evolution and current sheet formation converges. We also show the (conserved) energy density for a single Alfvén wave at 256 cells/wavelength (green dotted line), which does not undergo a cascade (*a*). The theoretical expectation of the energy dissipation for a fixed resistivity is indicated by grey dash–dotted lines, with the respective value of η shown below the respective line.

the estimated dissipation rate (dash–dotted lines) for force-free MHD runs with $\eta = 10^{-4}$, 5×10^{-5} and 10^{-6}. We conclude that for $\eta \leqslant 10^{-6}$ and resolutions of $\gtrsim 512^3$, Ohmic dissipation has a negligible effect on the initial 130 wave-crossings before the current sheets break-up. The energy dissipation rate agrees very well between ET-FFE (512^3 cells) and BHAC ($\eta = 10^{-6}$) for a resolution of 1024^3 cells. This result demonstrates that the formation and the thinning process of the current sheets, which occur between 100 and 125 wave-crossings, neither result in a significant energy decay nor in a violation of the ideal force-free constraints that would reduce the electromagnetic energy density (see also Appendix B). After approximately 125 wave-crossings, a steep decay is observed, which corresponds to the break-up of current sheets in figure 1, and energy is quickly dissipated at the grid-scale. We further conclude that the energy decay is a result of the cascade initiated by the wave interactions by showing that a single non-interacting Alfvén wave (green dashed line in figure 5*a*) shows no significant energy loss over 200 wave-crossings as indicated in figure 5(*a*). In figure 5(*b*), we show the MHD runs (BHAC) at $\sigma = 1$, 10 and 100, which correspond to smaller initial total electromagnetic energy, showing a similar evolution with a larger variability owing to the transfer of electromagnetic energy to fluid (kinetic and thermal) energy.

We analyse the evolution of the spectral magnetic energy $E_B(k)\,\mathrm{d}k = \sum_{\boldsymbol{k}\in\mathrm{d}k} \boldsymbol{B_k} \cdot \boldsymbol{B_k^*}$ for the resolved[4] ET-FFE is run at a resolution of 512^3 cells in figure 6. We observe a magnetic energy spectrum with a $E_{B_\perp}(k_\perp) \propto k_\perp^{-2}$ power law forming after 100 wave-crossings (green line in panel (*a,c*)) as a result of three-wave interactions. The power spectrum indicates that the turbulence in our simulations remains in the the weak regime $k_\parallel B_0 \gg k_\perp \delta B$ (Ng & Bhattacharjee 1997; Bhattacharjee & Ng 2001; Kuznetsov 2001; TenBarge *et al.* 2021). The transition from weak to strong turbulence is expected to occur after at least $\sim \chi^{-2} = 100$ wave-crossings. When the critical balance condition $k_\parallel B_0 \sim k_\perp \delta B$ becomes satisfied, such that the turbulence is in the strong regime, a $E_{B_\perp}(k_\perp) \propto k_\perp^{-3/2}$ energy spectrum is expected to form (Perez & Boldyrev 2008; Schekochihin, Nazarenko & Yousef 2012; Verdini & Grappin 2012). Owing to limited resolution and, hence, a limited inertial range, the wave energy starts to dissipate at the grid scale after $\sim$120 wave-crossings in our simulations such that the transition to strong turbulence is not captured here.

When the energy cascades to the highest k (or thinnest structures) after 100 wave-crossings, pronounced thin current sheets of high-amplitude current density form (see figure 1). Following Howes (2016), the emerging current sheets can be described by as few as the five lowest order modes. Only when smaller scale structures form in the thinning and breaking of current sheets, energy is transferred to higher order modes. This effect can be observed in the shift in the spectral evolution between 100 wave-crossings and the break-up point at 127 wave-crossings (see figure 6(*b,d*) for a zoom into the interval between 120 and 130 wave-crossings). At this point, the inertial range extends for almost two decades of $k_\perp$. Note that a current sheet itself results in a spectral index of -2 by assuming the Fourier transform of a (near)-step function (Burgers 1948). When the current sheets break-up at 127 wave-crossings, a maximally developed spectrum has formed as any thinner structures cannot exist on the numerical grid. Once the sheets break-up, the smallest scale (highest k) is reached by the cascade and the magnetic energy starts to dissipate at the grid-scale (roughly corresponding to $k_\perp > 100$). The spectral energy decays from here onward (orange and red lines).

The growth of turbulence at smaller scales and the subsequent decay is illustrated in the analysis of the χ parameter in figure 6(*c,d*). The steady-state expectation of $\chi(k_\perp)$ can be derived by assuming that the parallel cascade is negligible, and the weak turbulence spectrum shows that $\delta B_\perp^2/k_\perp \sim k_\perp^{-2}$ and hence $\chi = k_\perp v_\perp/(k_\parallel v_A) \sim \delta B_\perp k_\perp/(k_\parallel B_0) \sim k_\perp^{1/2}/k_\parallel \sim k_\perp^{1/2}$, indicated by the dashed line. The nonlinearity parameter clearly indicates that the turbulence remains in the weak regime $\chi < 1$ and develops towards $\chi \sim k_\perp^{1/2}$. The increasing nonlinearity parameter with $k_\perp$ and the cascade becoming more anisotropic suggests that, for higher resolutions, the transition to strong turbulence would be inevitable (Meyrand, Galtier & Kiyani 2016).

3.5. *Local weak turbulence properties*

In this subsection, we investigate the local properties of the turbulence to determine the local anisotropy of the spectrum. The Fourier analysis employed for the computation of the spectra cannot take into account the local properties of turbulence. It implicitly assumes the local mean magnetic field remains parallel to the initial field $\boldsymbol{B_0}$. However, each small scale eddy responds to the combined, local contribution of larger scale eddies. The weak

---

[4]In Appendix A, we determine the dispersion error for a single wave in a periodic 3-D box for a range of resolutions to verify that the spectra we obtained are reliable after many wave-crossings, when the original wave has decayed. This verification is necessary to avoid that, at the moment of current sheet formation, the low-k modes are lost owing to dispersion errors and the plasma is not in the weak turbulence regime anymore. We confirm in Appendix A that energy and dispersion errors are negligible for a single wave that is evolved for 200 wave-crossings and resolved by a few cells.

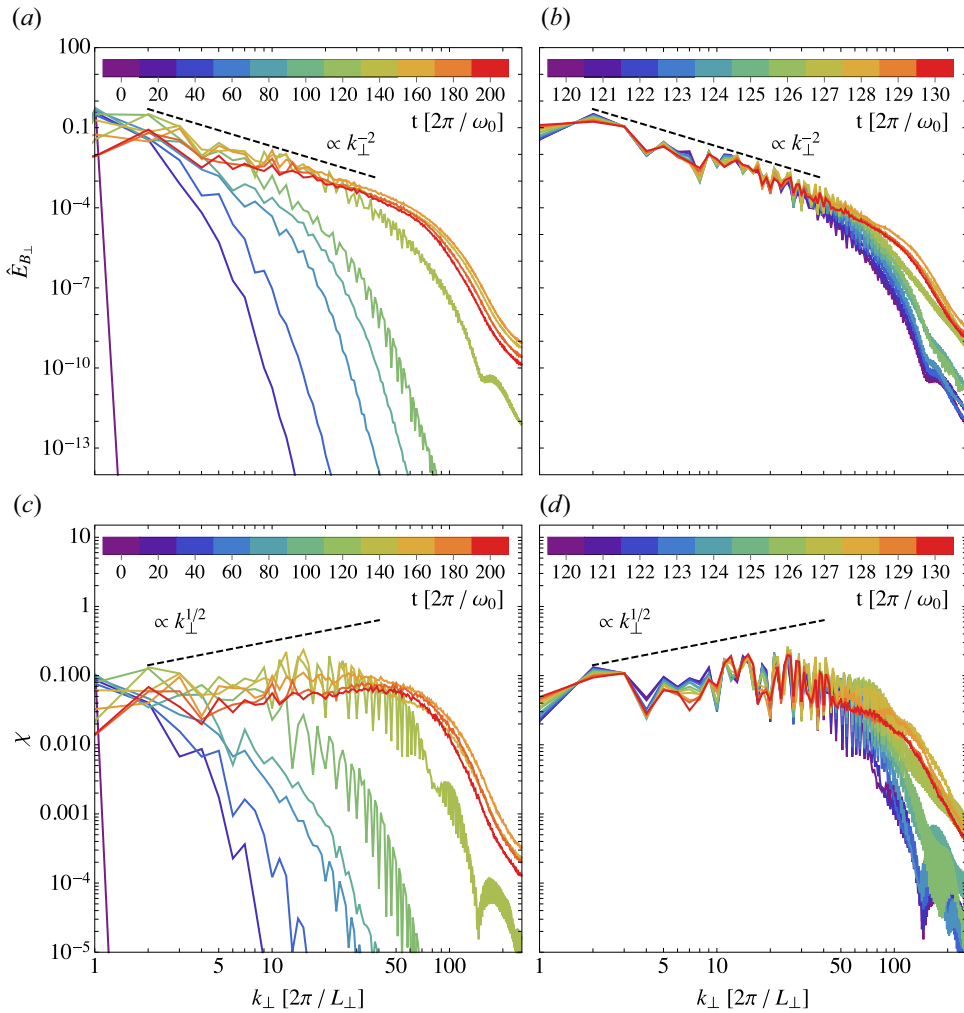FIGURE 6. Evolution of spectra (*a,b*) and non-linearity parameter χ (*c,d*) during the continuous wave interaction in the force-free limit. (*a*) $\hat{E}_{B\perp}$ spectra at every 20 wave-crossings with wave-amplitude $\chi = 10^{-1}$ and resolution $N_\perp = N_\parallel = 512$ grid-cells until 200 wave-crossings in ET-FFE. (*b*) Spectra at every wave-crossing between 120 and 130 wave-crossings. (*c,d*) Same analysis in time for the non-linearity parameter χ (reduced to its maximum value along slices of equal $k_\parallel$). There is a clear transition between 120 and 130 wave-crossings, when the current sheets thin and break-up after 127 wave-crossings, and an extended $\hat{E}_{B\perp} \propto k_\perp^{-2}$ spectrum develops. We note that the spectral evolution in the ET-FFE run at 512^3 resolution is similar to BHAC at 1024^3 resolution.

turbulence limit requires many collisions of counter-propagating waves to substantially deform the initial eddy, and an Alfvénic eddy propagates along the local, mean magnetic field. Accounting for the mismatch of local and global guide field requires one to define locally parallel and perpendicular cascades (Cho & Vishniac 2000; Maron & Goldreich 2001). To mitigate the effect of mixing parallel and perpendicular directions, we employ

second-order structure functions:

$$\delta B_i^2(\boldsymbol{l}) = \langle |B_i(\boldsymbol{r}+\boldsymbol{l}) - B_i(\boldsymbol{r})|^2 \rangle, \tag{3.1}$$

where l is a separation vector and angular brackets denote averages over all $\boldsymbol{r}$. These functions contain the information about the local spectrum $f(\boldsymbol{r_0}, \boldsymbol{l})$ at a given point $\boldsymbol{r_0}$, where $l \sim k^{-1}$. The local guide field for two points of an eddy of size l can be defined as

$$\boldsymbol{B}_{\text{guide}}(\boldsymbol{r}, \boldsymbol{l}) = \frac{\boldsymbol{B}(\boldsymbol{r}+\boldsymbol{l}) + \boldsymbol{B}(\boldsymbol{r})}{2}. \tag{3.2}$$

The shape of an eddy is given as $l_\parallel = \boldsymbol{l} \cdot \boldsymbol{B}_{\text{guide}}/|\boldsymbol{B}_{\text{guide}}|$, $l_\perp = (l^2 - l_\parallel^2)^{1/2}$, assuming that all eddies are isotropic in the field-perpendicular plane and neglecting effects of dynamical alignment and intermittency (Boldyrev 2005, 2006; Chandran, Schekochihin & Mallet 2015; Mallet, Schekochihin & Chandran 2015). The construction of (3.1) requires calculation of a six-dimensional (6-D) integral, and we employ a Monte Carlo method with a total of $N = N_0 n_x n_y n_z$ randomly chosen pairs of vectors to uniformly cover both the space of positions of eddies $\boldsymbol{r}$ and their sizes $\boldsymbol{l}$. Limits for the point-separation vectors l_i are chosen to be $(-n_i/2, n_i/2)$ to include the effects of the periodic boundary conditions in direction i. We set $N_0 = 30$ to decrease the shot-noise and confirm convergence of the results for $N_0 = 2, 5, 20$.

The 2-D structure functions for an ET-FFE run at a resolution of 512^3 cells are shown in figure 7, at time $t = 120$ $[2\pi/\omega_0]$, when thin current sheets have formed and are not yet broken up (see figure 1). All vectors $\boldsymbol{l}$ are split into 128 bins in both parallel and perpendicular directions. The white regions at larger $l_\parallel$ and $l_\perp$ do not contain any points as all separations larger than $l_i/2$ are prohibited owing to the periodic grid. The shape of the structure function is defined by the winding of magnetic field lines. A bright over-scaled feature at $l_\parallel \sim 0.5L_\parallel$ and $l_\perp < 0.5L_\perp$ is associated with the thinning current sheets: its amplitude grows while current sheets are being formed and disappears when current sheets break-up at $t \approx 128$. This feature appears both in the BHAC and ET-FFE results and is independent of how force-free violations are handled (see Appendix B).

The natural ability of this approach to consider local guide field variation allows us to measure a local angular anisotropy of the spectrum. To perform such a calculation, we split all point-separating vectors into 18 angular bins of $5°$ extension, measured with respect to the field-parallel direction ($0°$ is parallel to the guide field and $90°$ is perpendicular to it). In each bin, the intermediate range of $|\boldsymbol{l}|$ is approximated by a power-law function $\propto l^g$. The spectral index α is found using the relation $\alpha = -(g+1)$ (Monin & Yaglom 1999). The resulting anisotropy is shown in figure 8(a), and we observe that the spectrum is steeper in the parallel direction than in the perpendicular. For $\theta \to 0$, where θ is the angle between the local guide field and a chosen direction, the spectral index steepens to -3, which is the maximum that can be recovered using second-order structure functions as applied here (Farge & Schneider 2006). This result implies that there is no parallel cascade. For $\theta \gtrsim 20$, we find that the $E_{B_\parallel}$ spectrum is isotropic, which indicates the expected isotropy of a fast wave $E_{B_\parallel}$ spectrum (Cho & Lazarian 2002, 2003; Chandran 2005). In figure 8(b), we present the energy in modes parallel and perpendicular to the local guide field. This allows us to estimate the energy distribution in Alfvén and fast waves. The latter have parallel perturbations of the magnetic field while Alfvén waves have only perpendicular fluctuations $\delta \boldsymbol{B} \perp \boldsymbol{B}_{\text{guide}}$. Most of the magnetic energy is associated with Alfvén waves, and the fraction of energy in fast waves remains low at 1–5 %. For comparison, we overplot the energy distribution in the parallel and perpendicular components to the global guide field B_0: they are shown with dashed lines in figure 8(b). The fact that the energies match
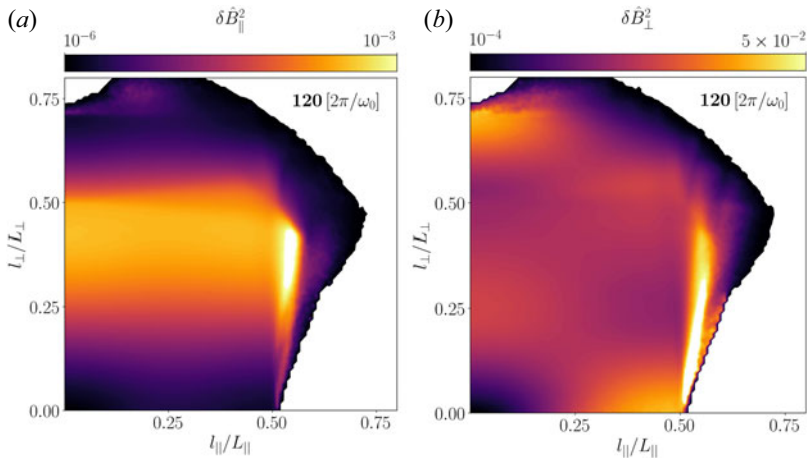
FIGURE 7. Two-dimensional structure functions for (*a*) $\delta\hat{B}_\parallel$ and (*b*) $\delta\hat{B}_\perp$ with respect to the local guide field, at time $t = 120 \, [2\pi/\omega_0]$ before the current sheets break-up. Here, $l_\parallel$ and $l_\perp$ are defined with respect to the local guide field. White regions at large l do not have any points owing to periodic boundary conditions. The bright feature at $l_\parallel/L_\parallel \approx 0.5$ corresponds to the current sheets.
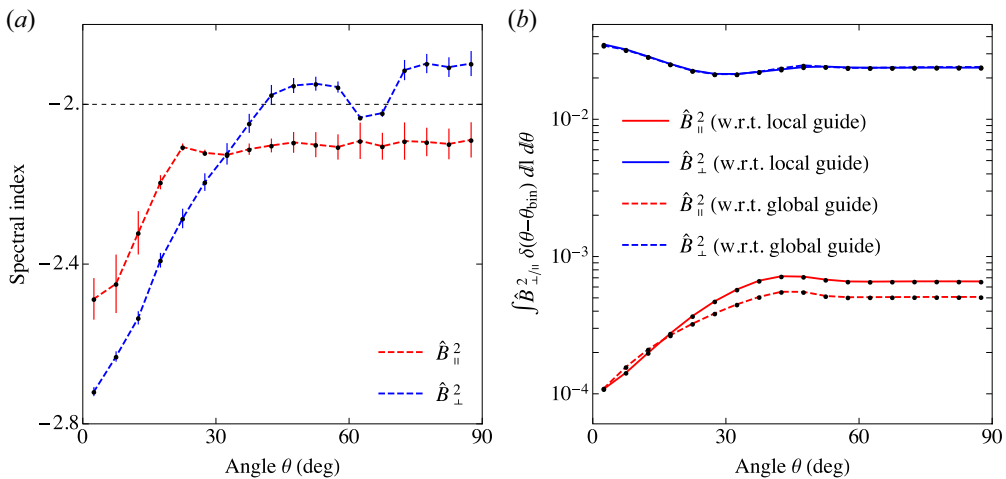

FIGURE 8. Angular properties for the turbulence at $t = 120 \, [2\pi/\omega_0]$: (*a*) the spectral index of the power-law spectrum as a function of angle between the *local* guide field and a chosen direction (θ); (*b*) the total energy contained in modes perpendicular and parallel to the local (solid lines) and global guide field (dashed lines) modes.

closely with respect to local and global fields highlights the nature of weak turbulence: as $\tau_{nl} \gg \tau_A$, eddies predominantly interact with the *global* guide field. The difference in the energy distribution of the parallel modes can be explained by projection of the energy in perpendicular modes on the parallel direction.

3.6. *Weak turbulence and current sheets in relativistic magnetohydrodynamics*

In this section, we compare the formation of current sheets in weak MHD turbulence to the force-free results presented in the previous sections. In figure 9, we compare force-free
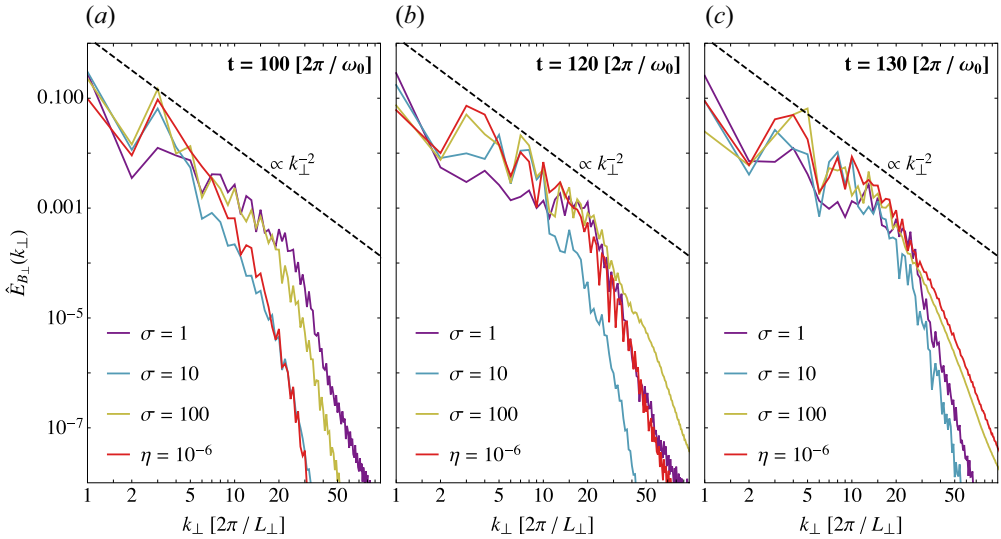
FIGURE 9. Evolution of spectra during the continuous wave interaction for different magnetizations. The $\hat{E}_{B_\perp}$ spectra at 100 ± 2, 120 ± 2 and 130 ± 2 wave-crossings at resolution $N_\perp = N_\parallel = 512$ grid-cells for runs at $\sigma = 100$, 10 and 1 and force-free MHD in BHAC. The spectra are averaged over five wave-crossings. For the force-free MHD run, we set $\eta = 10^{-6}$. The $\hat{E}_{B_\perp} \propto k_\perp^{-2}$ spectra develop at 100 wave-crossings.

MHD and ideal MHD spectra obtained with BHAC for $\sigma = 1$, 10 and 100 at 512 cells per initial wavelength, which shows that in all four cases, a $E_{B_\perp}(k_\perp) \propto k_\perp^{-2}$ magnetic energy spectrum forms and then a transition occurs between 100, shown in panel (*a*), and 130, shown in panel (*c*), wave-crossings induced by current sheet formation and break-up. After 120 wave-crossings, shown in panel (*b*), the total electromagnetic energy starts to decay (see figure 5*b*). Owing to energy transfer between electromagnetic and hydrodynamic (kinetic and thermal) components, the onset time of the steep decay and therewith the development of the spectrum differs slightly for varying σ, where $\sigma = 100$ corresponds most closely to the force-free MHD result.

We show the structure of the forming current sheet shortly before it breaks-up at $t = 118\ [2\pi/\omega_0]$ in the $\sigma = 100$ MHD run in BHAC in figure 10(*a*), similar to the force-free current sheet in figure 1. The sheet breaks up at $t = 123\ [2\pi/\omega_0]$. A pressure gradient contributes to the force balance to sustain current sheets in the relativistic MHD simulations. For smaller σ, the current sheets have a smaller aspect ratio and they have an effectively lower Lundquist number owing to the lower Alfvén speed and length. The thinning rate (shown in panel (*c*)) of the current sheet is very similar to the force-free result, which converges between 512^3 and 1024^3 grid points (see figure 3).

4. Collisions of Alfvén wave packets

In this section, we illuminate the development of current sheets in a more realistic setting of collisions between initially separated Alfvén wave packets (see e.g. Verniero & Howes 2018; Verniero *et al.* 2018; Li *et al.* 2019; Li, Beloborodov & Sironi 2021). Owing to the localization of wave packets, we expect the character of secondary modes to differ significantly from the results presented in § 3 (cf. Verniero *et al.* 2018). In the following sections, we will dissect the secondary mode structure emerging during the interaction of
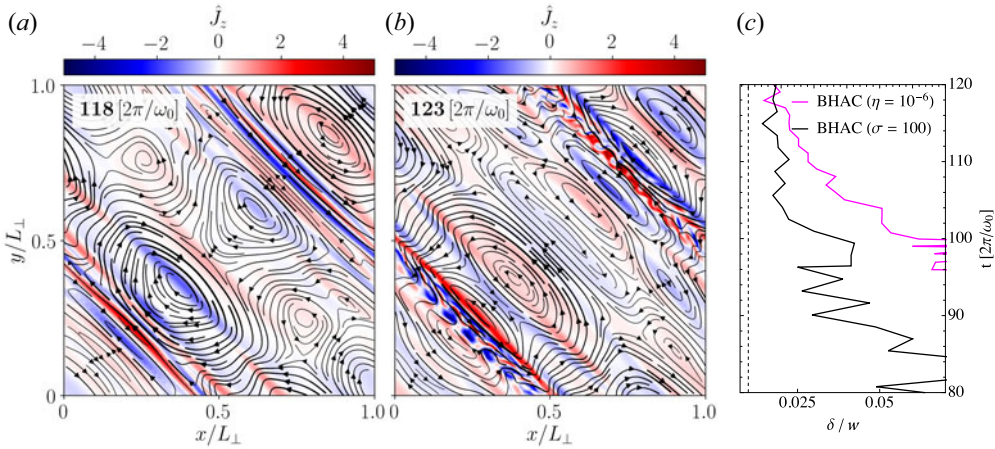
FIGURE 10. Current sheets form between elongated eddies in the MHD run for $\sigma = 100$ with BHAC. (*a,b*) Out-of-plane current density $\hat{J}_z = [\nabla \times \boldsymbol{B}]_z/(k_\perp B_0)$ at 118 and 123 wave-crossings, respectively, before and after the break-up of the current sheet. (*c*) Current sheet's aspect ratio δ/w measured as the full-width at half maximum of the current density normalized by its approximately constant width $w \approx 2\pi$ versus wave-crossings for both the $\sigma = 100$ and force-free runs in BHAC at 512^3 grid points.

Alfvén wave packets in the relativistic limit. Further, we probe if the finite extension and interaction time of the wave also results in rapid dissipation of electromagnetic energy in current sheets, as we proposed in § 3.2.

4.1. *Packet initialization*

To allow for a direct comparison with the results of the previous sections, we only modify the wave initialization described in § 3.1 in two key aspects. First, the cubic box is extended along the direction parallel to the guide field, with $L_\parallel = 10\pi$. This choice allows us to separate the waves in packets while the choice of $k_\parallel$ re-scales the wave in the elongated domain. Second, the two Alfvén waves are localized along the (parallel) z-direction by window functions with a Gaussian profile (cf. Verniero *et al.* 2018):

$$w(z) = \exp\left[-\left(\frac{z - z_0}{\Delta_z}\right)^p\right] + \exp\left[-\left(\frac{z - z_0 + L_\parallel}{\Delta_z}\right)^p\right] + \exp\left[-\left(\frac{z - z_0 - L_\parallel}{\Delta_z}\right)^p\right].$$
$$(4.1)$$

We choose a window width of $\Delta_z = L_\parallel/4\pi$ and the power $p = 2$. The two waves are localized at the window centres $z_{0-} = L_\parallel/4$ and $z_{0+} = 3 \times L_\parallel/4$. Initial phase shifts δ_- and δ_+ align the waves symmetrically in their respective windows. For the tests presented in this section, we fix the nonlinearity parameter to $\chi = k_\perp \delta B_\perp/(k_\parallel B_0) = 0.25$. Hence, though the wave amplitudes are comparable to the continuous set-up (§ 3), the nonlinear time in the localized set-up is drastically reduced to $\chi^{-2} = 16$ wave interactions. This choice is beneficial for this numerical exploration. In contrast to the overlapping waves in § 3, the elongated domain requires each wave packet to propagate significant distances between the interaction events. Decreasing the nonlinear time thus allows us to reach the relevant stages of turbulence during a reasonable computational time.

We present insight into the collisional dynamics of localized Alfvén waves by combining two specific wave types: AW_1, where $k_\parallel = 2\pi/L_\parallel$ with an initial wave
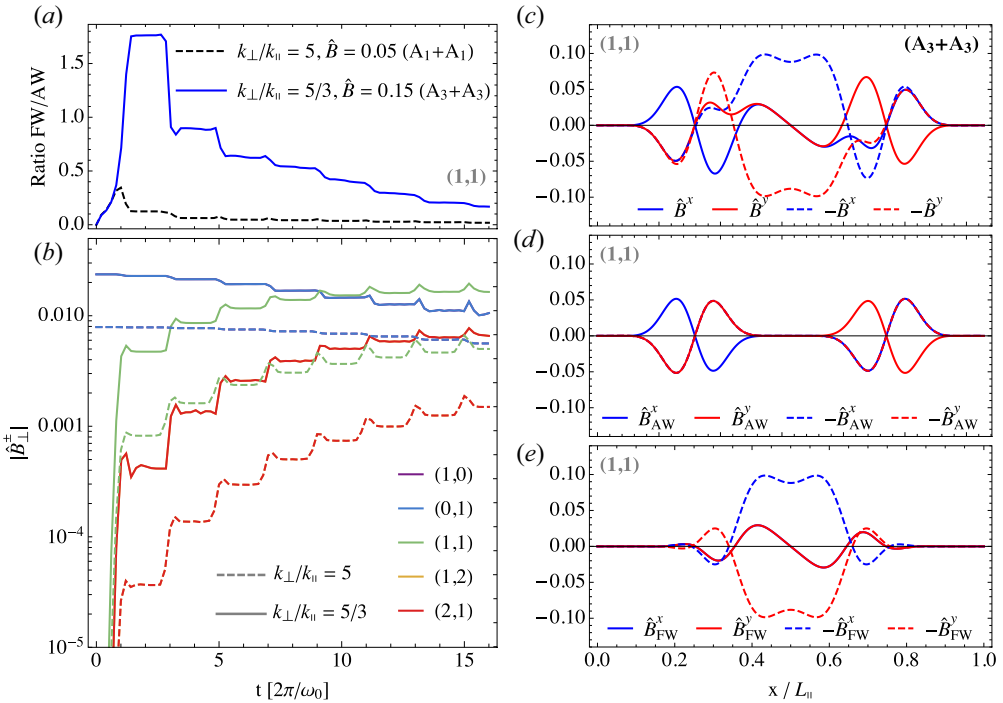
FIGURE 11. Evolution of individual modes during the interaction: (*a*) comparison of the AW_3 + AW_3 and $AW_1 + AW_1$ collisions for the intermediate resolution of $256^2 \times 320$; (*b*) decay of the primary modes $(1, 0)$ and $(0, 1)$ with sustained growth of the $(1, 1)$ mediator mode as well as the secondary modes $(2, 1)$ and $(1, 2)$. The respective ratio between the total energy stored in the Alfvén and in the fast channel of the $(1, 1)$ mode is displayed in panel (*a*). Exemplary decomposition of the $(1, 1)$ mode by its polarization for the $AW_3 + AW_3$ collisions: (*c*) total magnetic field along the centre of the domain; (*d*) projection into the Alfvén mode; (*e*) projection into the fast mode. An animation of the $(1, 1)$ mode structure and dynamics during the first interaction cycles is provided in Media Supplement C (2021) and Media Supplement H (2021).

amplitude of $\delta B_\perp / B_0 = 0.05$ and $k_\perp / k_\parallel = 5$; and AW_3, where $k_\parallel = 3 \times 2\pi / L_\parallel$ with an initial wave amplitude of $\delta B_\perp / B_0 = 0.15$ and $k_\perp / k_\parallel = 5/3$. Specifically, we examine the interactions $AW_1 + AW_1$ and $AW_3 + AW_3$ to understand the evolution of higher order modes (figure 11). We then focus on comparing the interactions $AW_1 + AW_3$ and $AW_3 + AW_3$ by closely following the effect of shearing modes and the ensuing dissipation of electromagnetic energy (figure 12). The wave vectors differ to those of the continuous case (§ 3) in their parallel component: $k_\parallel$ is both re-scaled and filtered by the window function, which results in the initial wave packets having a broad spectrum of $k_\parallel$ modes rather than $k_\parallel = \pm 1$. It is, thus, simplest to limit the representation of modes to the components of $k_\perp$, namely, $(k_x L_\perp, k_y L_\perp) = (1, 0)$ for $\boldsymbol{k}_1^+$ and $(0, 1)$ for $\boldsymbol{k}_1^-$. The mediator mode $\boldsymbol{k}_2^0$ is then $(1, 1)$, with tertiary modes $(2, 1)$ for $\boldsymbol{k}_3^+$ and $(1, 2)$ for $\boldsymbol{k}_3^-$. The reality condition of the Fourier transform also implies a mirrored energy in the modes $(-1, 0)$ for $\boldsymbol{k}_1^+$ and $(0, -1)$ for $\boldsymbol{k}_1^-$, as well as in their respective superpositions. The interaction of Alfvén wave packets proceeds through the coupling of these modes in (superficial) analogy to the continuous case presented in § 3. The details of this mechanism, however, reveal some notable subtleties.
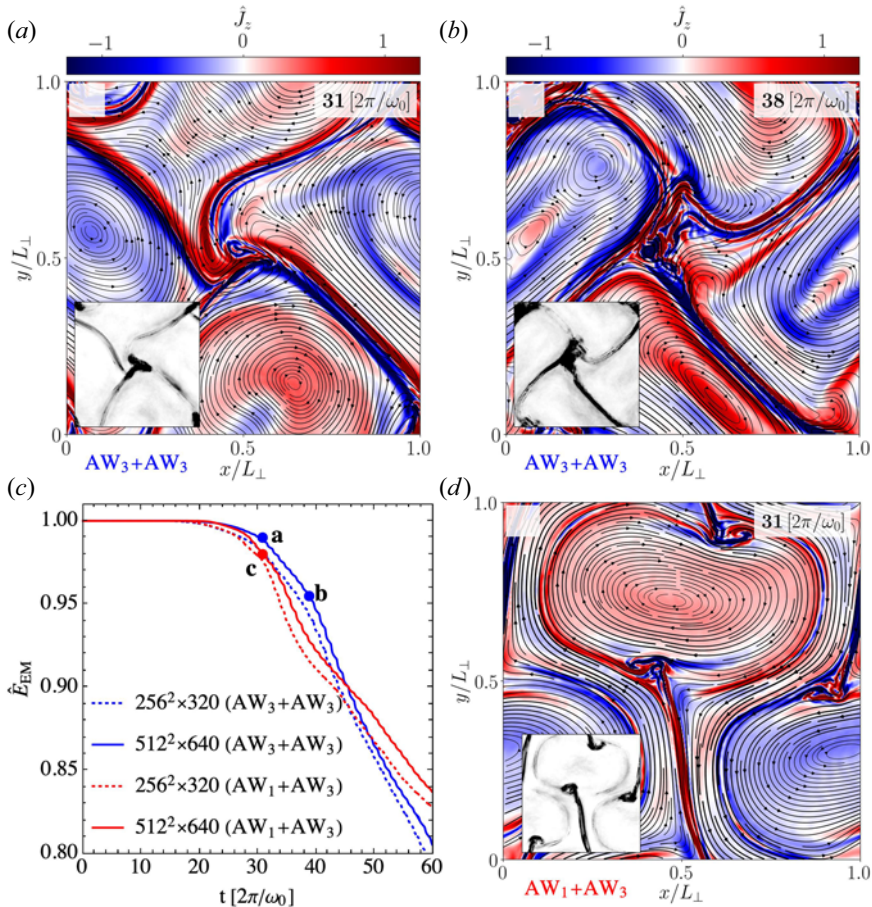
FIGURE 12. Decay of (normalized) total wave energy $\hat{E}_{EM} = E_{EM}/E_{EM,t=0}$, with $E_{EM} = (B - B_0)^2 + E^2$ driven by the reconnection zones and current sheets induced by the shearing action of the secondary mode. (*a*,*b*,*c*) Visualization of the out-of-plane current density $\hat{J}_z = [\nabla \times \boldsymbol{B}]_z/(k_\perp B_0)$ and field composition of the wave packets at different times in high resolution as indicated in the energy plot. The insets provide an impression of the *z*-averaged non-ideal field marker $\boldsymbol{E} \cdot \boldsymbol{B}/B^2$. Regions of strong (numerical) diffusion of non-ideal electric fields (i.e. violations of the force-free conditions) appear in dark shades. Such locations include Y-points, such as the anchor points of the shearing motion, and current sheets. (*d*) Evolution of the wave energy (normalized) for interactions of different wave types and resolutions. Animations of the interaction dynamics are provided in Media Supplement D (2021) and Media Supplement E (2021).

4.2. *Interaction dynamics*

Two localized Alfvén waves create linear fast waves as well as linear Alfvén waves during their interaction, and we exploit the mode structure in Fourier space to conduct the analysis of secondary modes. Such a transformation allows us to select specific coordinates of $k_\perp$ and $k_\parallel$ to identify and distinguish Alfvén and fast modes. As we show in figure 11(*b*), the interacting primary modes $(1, 0)$ and $(0, 1)$ transfer their energy to the $(1, 1)$ mediator mode and, subsequently, to the tertiary waves $(1, 2)$ and $(2, 1)$. The energy transfer is strongest during each collision, as one can infer from the step-like growth in figure 11 (*b*).
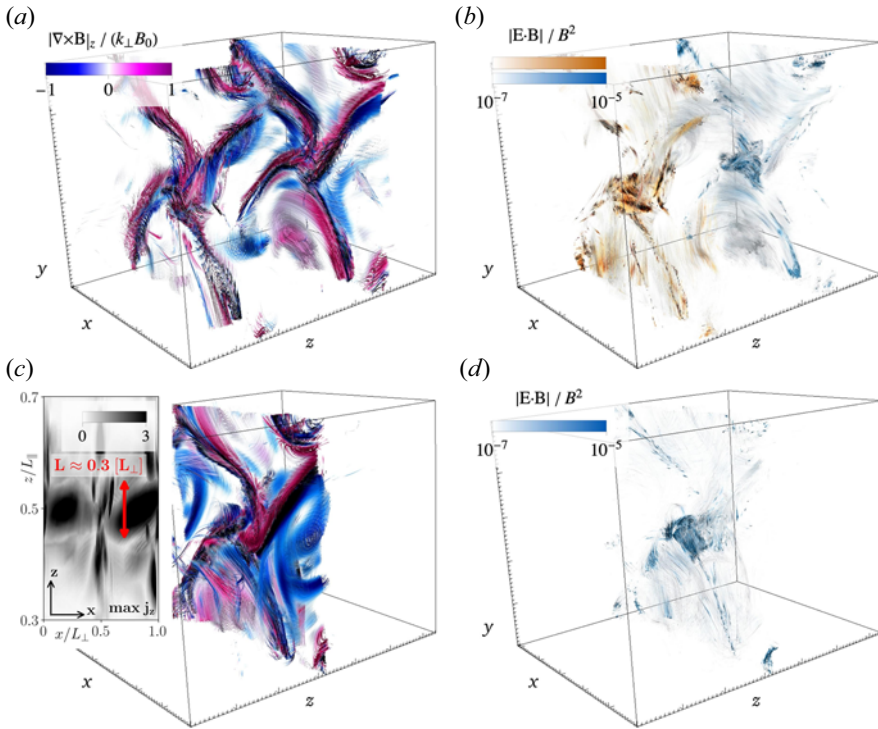
FIGURE 13. Three-dimensional impressions of the $AW_3 + AW_3$ collision during a phase of packet separation ($t = 31$ $[2\pi/\omega_0]$, (*a,c*)) and the subsequent interaction ($t = 31.5[2\pi/\omega_0]$, (*b,d*)). We colour field lines along $\hat{B}$ by the current density $|\nabla \times B|_z/(k_\parallel B_0)$ (*a,c*) and by the local non-ideal electric field marker $E \cdot B/B^2$ (*b,d*). The vortex-like anchor points of the shear (cf. figure 12) are extended along the z-direction and coincide with regions of non-ideal diffusion. The inset in panel (*c*) shows a top view of the maximum current density to estimate the depth of the current structures. The different colours in panel (*b*) distinguish between field lines as seeded in the two central planes of the displayed wave packets. A 3-D animation of the dynamics in the interaction region can be found in Media Supplement F (2021).

In analogy to Verniero & Howes (2018), we examine two key characteristics of the secondary $(1, 1)$ mode: field polarization and wave dispersion. Force-free linear Alfvén waves with dispersion $\omega(k) = \pm k_\parallel$ are composed of an electric field along $k_\perp$ and a magnetic field along $\hat{z} \times k_\perp$. For the $(1, 1)$ mode, this reduces to the following polarization and group velocity

$$[\text{AW}] \quad B^x = \pm E^y \quad B^y = \mp E^x \quad \frac{\partial \omega}{\partial k_\parallel} = \pm 1. \qquad (4.2a\text{--}d)$$

Force-free fast waves with dispersion $\omega(k) = \pm|k|$ are composed of an electric field along $k_\perp \times \hat{z}$ and a magnetic field along $k \times (k_\perp \times \hat{z})$. For the $(1, 1)$ mode, this reduces to the following polarization and group velocity

$$[FW] \quad B^x = \mp \frac{k_\perp}{|k|} E^y \quad B^y = \pm \frac{k_\perp}{|k|} E^x \quad \frac{\partial \omega}{\partial k} = \pm 1. \qquad (4.3a\text{--}d)$$

Both Alfvén waves and fast waves are relevant for the relativistic interaction of localized wave packets, and we present a summary of our detailed investigation in the following.
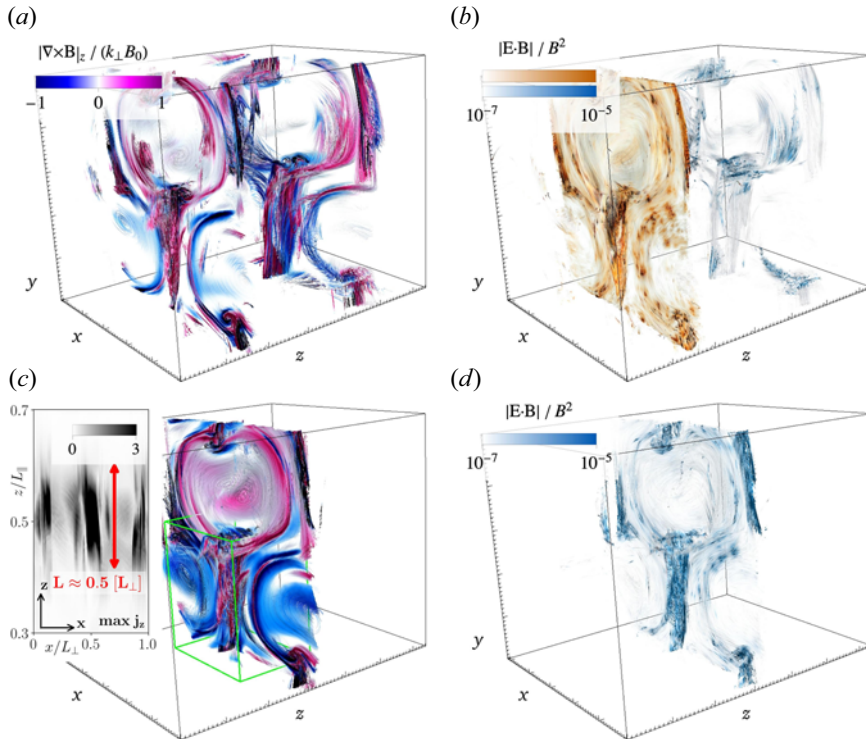
FIGURE 14. Three-dimensional impressions of the $AW_1 + AW_3$ collision in analogy to figure 13 ($t = 31$ [$2\pi/\omega_0$], (a,c)); $t = 31.5$ [$2\pi/\omega_0$], (b,d)). A current layer separates two equally polarized eddies. It coincides with field reversals, strong currents and significant dissipation by emerging non-ideal electric fields. A detailed outline of the reconnection region (green box) with realistic proportions is presented in figure 15. A 3-D animation of the dynamics in the interaction region can be found in Media Supplement G (2021).

For a fixed $\chi = k_\perp \delta B/(k_\parallel B_0)$, a smaller ratio $k_\perp/k_\parallel$ corresponds to a larger $\delta B/B_0$ such that the system is driven away from the reduced MHD limit $\delta B_\perp/B_0 \sim k_\parallel/k_\perp \ll 1$ (Paper I). Hence, the amount of energy stored in the FW increases for a smaller ratio $k_\perp/k_\parallel$ (as we show in figure 11a). During the initial phase of the interaction, fast waves in the $(1, 1)$ mode show a progressive decay in energy after each primary wave collision. In contrast, $(1, 1)$ Alfvén waves incrementally increase in energy during each primary interaction event and conserve their energy in between. Fast waves effectively propagate as spherical waves in a periodic domain (see also Media Supplement C 2021; Media Supplement H 2021). They, thus, continuously interact with Alfvén waves and other fast waves; energy is transferred out of the $(1, 1)$ mode at a higher rate than for their Alfvénic counterpart. Figure 11(c,d,e) probes the decomposition of the wave fields in the $(1, 1)$ mode along the aforementioned characteristic directions. For the Alfvén mode (analysed in figure 11d), it is then straightforward to identify the field polarizations derived in (4.2a–d). However, a quantitative analysis of the group velocity as well as the field polarizations of the fast wave (4.3a–d) is more difficult. This intricacy is rooted in the finite spectrum of $k_\parallel$ owing to the localization of the initial pulses, i.e. $k_\parallel$ is not a constant. A careful decomposition of wave modes for each individual $k_\parallel$ is required to confirm the remaining dispersion properties locally in Fourier space. We conducted such a brute-force validation. It shows

that the $(1, 1)$ mode is, indeed, the superposition of a linear Alfvén wave and a linear fast wave.

We note that in contrast to the continuous interaction of AWs, the localized $(1, 1)$ mediator mode is a superposition of waves with a finite spectrum in $k_\parallel$. More specifically, it is not a nonlinear fluctuation with $k_\parallel = 0$. This distinction of spectral components is the key to understanding the localized AW + AW interaction. Counter-propagating Alfvén waves interact resonantly and satisfy the matching conditions

$$\boldsymbol{k}_1^+ + \boldsymbol{k}_1^- = \boldsymbol{k}_2, \quad \omega_1^+ + \omega_1^- = \omega_2. \tag{4.4a,b}$$

For these conditions to result in an outgoing AW, as identified in (4.2*a–d*), one of the incoming modes is required to have $k_\parallel = 0$. Such a combination is possible when one wave packet of a finite $k_\parallel$ spectrum interacts with the $k_\parallel = 0$ component of another wave packet (Ng & Bhattacharjee 1996). The resulting AW would then have a distribution of $k_\parallel$ that matches the primary mode; we find that this is indeed the case. An interaction between primary modes across the full spectral range of $k_\parallel$ also results in an outgoing FW. Owing to the addition of spectral ranges, the FW should have an accumulation of power at $k_\parallel = 0$. We observe this feature consistently in our analysis.

The interaction of continuous counter-propagating AWs with the symmetry of constant and oppositely signed $k_\parallel$ has a unique solution to the resonance condition of (4.4*a,b*). Namely, it yields the nonlinear fluctuation $(1, 1, 0)$. The localization of waves in packets extends the spectrum of $k_\parallel$ along a finite range and the symmetry in the resonance is broken. In contrast to the continuous interaction (§ 3), the secondary mode has a linear Alfvén wave character and propagates according to the dispersion relation given above. During each interaction of the wave packets, energy is transferred to the secondary (and higher order) modes. The secondary mode manifests through shearing of the magnetic field. While, initially, wave packets form elongated tubes along their respective $k_\perp$, the persistent shearing stretches these tubes, gradually compressing them (cf. figure 12). The interaction of waves with symmetric $k_\parallel$ induces the $(1, 1, 0)$ oscillating shear mode. Thus, depending on the combination of initial $k_\parallel$, as to say, of the wave packets AW$_1$ and AW$_3$, the shearing motion can be continuously progressing (for non-symmetric $k_\parallel$) or oscillating (for symmetric $k_\parallel$).

In the case of AW$_1$ + AW$_1$, the oscillation of the shearing process prevents the compression of anti-parallel field lines in between eddies into current sheets. However, elongated eddies, e.g. at $x \approx 3\pi/2, y \approx \pi/2$ at $t = 31$ $[2\pi/\omega_0]$ in figure 12(a), develop and form pancake-like current sheets, e.g. at $x \approx 4\pi/3, y \approx \pi/3$ at $t = 31$ $[2\pi/\omega_0]$ in figure 12(b). Prominent non-ideal electric fields form at these locations. The signatures of current sheets at later times (figure 12(b)) can be associated with a mild steepening of the energy dissipation. The shearing and stretching of larger eddies into reconnection layers are a characteristic of both continuous and localized Alfvén wave interactions.

In analogy to the case of continuous interaction (§ 3), elongated eddies can form long current sheets that will eventually break up (cf. § 3.2). As in the previous analysis of continuous interactions, we associate the onset of dissipation of cascaded energy with the emergence and break-up of current sheets. We identify sheets of strong current density, prominent non-ideal electric fields, and field reversals in the AW$_1$ + AW$_3$ case (figure 12(c)) owing to field line compression between two eddies at $x \approx \pi, y \in [0, \pi]$ in figure 12(c). They emerge and decay at the same time as we observe a change in slope in the energy evolution.

We note that at the relatively high value of χ for wave packet simulations, while we have seen a persistence of the $E_{B_\perp}(k_\perp) \propto k_\perp^{-2}$ spectrum despite the presence of intermittency
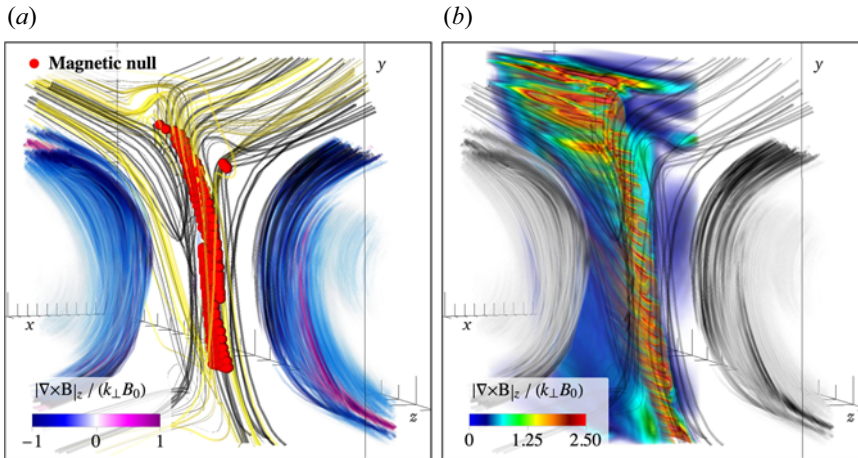
FIGURE 15. Detailed 3-D outline of the reconnection region during the $AW_1 + AW_3$ collision (as presented in figure 14). (*a*) Magnetic null points (red spheres, where we removed the initial background field B_0 along $\hat{z}$) between eddies of the same polarity. Yellow field lines are seeded at the locations of the strongest currents, black field lines have a slight offset to these seeds in the perpendicular plane. (*b*) Volume rendering of the strongest currents (as we showed for the continuous case in figure 4).

(in the form of current sheets), we begin to see some features of a transition to strong turbulence (Meyrand *et al.* 2016) which call for further studies.

We conclude this section by studying 3-D profiles of the wave interactions of the $AW_3 + AW_3$ as well as the $AW_1 + AW_3$ collision in figures 13 and 14. In these figures, we colour a large number of field lines seeded in planes at the centre of the respective wave packets (or their superposition) by the current density $|\nabla \times \boldsymbol{B}|_z/(k_{\parallel}B_0)$ in panel (*a,c*) and by the local non-ideal electric field marker $\boldsymbol{E} \cdot \boldsymbol{B}/\boldsymbol{B}^2$ in panel (*b,d*). First, we note that the wave magnetic field is well localized even after several tens of interactions. Second, possible 3-D reconnection sites emerge in the form of bulged eddies (figure 13) or current sheets with varying depth (figure 14). These structures exist individually in each wave packet and interact progressively, enhanced by the shearing action of the secondary mode. The z-extensions of non-ideal structures is a fraction of the initial window-size Δ_z in the case of the bulged eddies. Current sheet structures, however, have a significant depth of the order of (and even slightly above) the initial window-size Δ_z. Figure 15 dissects the topology of the current sheet emerging during the $AW_1 + AW_3$ collision, which shows some anti-parallel field lines and some reconnecting field lines. We mark the localized layer of magnetic null points with red dots (i.e. points with reversals of all field components, where the initial background field B_0 along $\hat{z}$ is removed).

Collisions of localized Alfvén waves are efficient mediators of energy conversion to smaller scales (perpendicular to the guide field) and powerful drivers of nonlinear energy cascades. The mixing of wave packets with different ratios of $k_{\perp}/k_{\parallel}$ significantly changes the interaction dynamics by suppressing the oscillatory (1,1,0) shear mode. Mixing effectively triggers episodes of very fast dissipation of electromagnetic energy mediated by the break-up of elongated current sheets. As in the continuous case (cf. figure 4), the current sheet ripples as it is stretched between elongated eddies and eventually breaks up into smaller (turbulent) structures. Mixing waves of different $k_{\perp}/k_{\parallel}$ is an appealing case for

a future exploration of current sheet formation and the transition into the strong turbulence regime for the interaction of overlapping Alfvén waves in high-resolution runs.

5. Conclusions

In this work, we show that the interaction of overlapping and counter-propagating Alfvén waves in highly magnetized relativistic plasma results in an anisotropic energy spectrum $E_{B_\perp}(k_\perp) \propto k_\perp^{-2}$. The weak turbulence energy cascade occurs owing to the scattering of Alfvén waves dominated by three-wave interactions. The nonlinear dynamics of Alfvén wave collisions provide a natural mechanism for the development of current sheets in plasma turbulence. Turbulent eddies that form through constructive interference of the primary Alfvén waves and nonlinearly generated modes become elongated and stretched on nonlinear timescales $\sim \chi^{-2}$, until they transiently form current sheets. The current sheets undergo a thinning process owing to the compression of the eddies, which results in a final thickness $\delta/w \approx 0.01$ before they break-up into small-scale turbulent structures. Analysing the electromagnetic energy evolution of the system, we find that the turbulent cascade reaches the grid scale at the moment the current sheets break-up, at which time the energy dissipates dramatically. We suggest that magnetic reconnection in the current sheet regions is a viable mechanism through which energy dissipates in these highly relativistic and magnetically dominated fluid systems.

The presented results show that the fundamental properties of Alfvén wave collisions, as observed in the idealized case of periodic and overlapping waves, persist under the more realistic conditions of localized wave packets. The evolution and interaction of the wave packets occurs during their overlap only, and the Alfvén component of the wave packets remains localized along the guide magnetic field before and after their collision. As a consequence, packet collisions are, in many ways, similar to the continuous wave collisions. Especially, strong dissipation of electromagnetic energy in current sheets starts to develop at nonlinear timescales of the order of χ^{-2}. In contrast to the continuously overlapping waves, the mediator of the turbulent cascade that transfers energy to the smallest scales is not a purely nonlinear magnetic mode, but a combination of linear Alfvén and fast waves.

In fact, fast waves are absent in the non-relativistic limit (Verniero & Howes 2018; Verniero *et al.* 2018); thus, despite a multitude of similarities between Alfvénic turbulence in the Newtonian versus relativistic limits, this notable difference provides at least one alternative path for the turbulence to dissipate its energy because the linear fast modes can travel across field lines. Regardless, as in the Newtonian limit, the secondary Alfvén mode is essentially a shear in the magnetic field that propagates along the guide field and shears the counter-propagating Alfvén wave packets. In addition, for a fixed $\chi = k_\perp \delta B/(k_\parallel B_0)$, a large ratio of $k_\perp/k_\parallel$ results in a smaller amount of energy stored in the fast waves, in accordance with the asymptotic solutions in Paper I. We have demonstrated that current sheets form during the interaction of two packets for different ratios of $k_\perp/k_\parallel$ and that they act as the main dissipation sites.

Although the force-free limit of the MHD equations is technically invalid inside a reconnecting current sheet (where $E > B$ or $\boldsymbol{E} \cdot \boldsymbol{B} \neq 0$) and it cannot describe the physical effects of magnetic reconnection and resistive dissipation, it does contain the minimal ingredients that lead to the anisotropic cascade and the development and thinning of current sheets in relativistic plasma turbulence. We have validated our results for finite magnetization in magnetically dominated ideal relativistic MHD. We suggest that the emergence and dynamic decay of current sheets is driven by the global dynamics of wave interactions. We verify that at the highest presented resolutions, the small structures we identify are not dominated by numerical diffusion or dispersion errors (cf. Appendix A).

To validate our findings, we emphasize, once more, the striking similarity of results from two independent, vastly different force-free MHD algorithms. To study current sheets as dissipation sites in interacting Alfvén waves in more depth, we will in the future carry out relativistic resistive MHD simulations (Ripperda *et al.* 2019*a*,*b*) and evolve test particles to capture magnetic reconnection as a particle heating and acceleration mechanism (Ripperda *et al.* 2017*a*,*b*, 2018).

Though obtained in the context of fundamental plasma physics, the results are vital for the magnetospheres of astrophysical compact objects. Turbulence in black hole accretion disks may launch Alfvén waves that propagate from the disk into the corona (Thompson & Blaes 1998; Chandran *et al.* 2018). Such waves may propagate away from the disk into regions with varying magnetization and reflect, after which the interaction with other waves may result in a turbulent cascade. At this point, a significant fraction of the wave energy can dissipate within a few scale heights of the disk. The current sheets formed by relativistic Alfvénic turbulence, as found in this work, may provide the main dissipation sites of magnetic energy through magnetic reconnection, which yields a promising mechanism for explaining the X-ray emitting coronae that are observed around luminous active galactic nuclei. Even in the weak turbulence regime ($\chi < 1$) explored here, a large reservoir of magnetic energy is available in the turbulent fluctuations $\delta B_\perp$ in magnetized accretion disk coronae. The turbulence in black hole accretion disks may even be in the strong turbulence limit (i.e. $\delta B_\perp / B \geqslant 1$), a regime we explore in another study (Chernoglazov, Ripperda & Philippov 2021).

The interaction of wave packets is equally relevant in neutron star magnetospheres. Magnetar flares can excite strong Alfvén waves in the highly magnetized magnetosphere. The wave packets can dissipate their energy through interactions with reflecting waves (Li *et al.* 2019), or they may dissipate their energy in the neutron star's crust (Li & Beloborodov 2015). They can also convert to fast modes which are not confined to the magnetic field and can escape from the magnetosphere (cf. Yuan *et al.* 2020*b*). A turbulent cascade of large amplitude Alfvén waves in the magnetosphere can lead to plasma heating and X-ray emission. The fraction and rate of dissipation constrains the duration and flux of the observed X-ray emission following a magnetar flare. On another note, pulsar glitches may launch Alfvén waves into the magnetosphere, which can lead to enhanced current and pair production that quenches the radio emission (Bransgrove *et al.* 2020; Yuan *et al.* 2020*a*). The lifetime, dissipation channel and the ratio between turbulent Alfvén and fast modes (dependent on the $k_\parallel / k_\perp$ ratio of the primary waves, as we show in §3) constrains the duration of the observed radio emission anomaly. We argue in this work that it is essential to study wave interaction in neutron star magnetospheres in three dimensions to determine the fraction of energy that can escape through fast modes in future magnetospheric modelling.

Finally, looking beyond the validity of our models, we note that the low density of the plasma in the magnetospheres of neutron stars and black holes results in a mean free path for collisions that is much larger than the length scales of turbulent fluctuations, often even exceeding the system size. Thus, plasma can be considered collisionless, and turbulent dynamics and dissipation are governed by kinetic physics. The MHD approximation fails in this regime and cannot capture the collisionless kinetic physics, potentially resulting in non-thermal radiation that is typically observed. Throughout the results presented in this manuscript, we observe strong guide field current sheets emerging as a result of Alfvén wave collisions. In this regime, the energy available for plasma energization is limited, which results in significantly steeper power-law spectra shown by the first-principles particle-in-cell simulations of Werner & Uzdensky (2017). By using gyrokinetic simulations, TenBarge & Howes (2013) and Howes *et al.* (2018)

showed that plasma heating is indeed correlated with the emergence of current sheets. Landau damping plays an essential role in the spatially intermittent energization of particles through dissipation of turbulent fluctuations. Understanding the mechanism that energizes the plasma in black hole accretion disk coronae and neutron star magnetospheres is an important problem in high-energy astrophysics. Force-free and relativistic MHD simulations capture the essential global dynamics to describe a weak turbulence cascade and the formation of current sheets that can act as dissipative regions in highly magnetized plasma as found in compact object magnetospheres and coronae.

Editor Alex Schekochihin thanks the referees for their advice in evaluating this article.

Declaration of interests

The authors report no conflict of interest.

Appendix A. Numerical convergence of the force-free MHD schemes

We test our newly implemented force-free algorithm in BHAC for an Alfvén wave propagating in the z-direction along the guide field $B_z = B_0$ with wave vector $\boldsymbol{k} = (1, 0, 1)$, for 200 wave-crossings through a box of size $(2\pi, 2\pi, 4\pi)$ with $N_{\lambda,z}$ cells per wavelength and resolution $(N_\perp, N_\perp, N_\parallel)$, where $N_{\lambda,z} = N_\perp = 0.5N_\parallel \in [8, 16, 32, 64, 128, 256, 512]$. We measure the numerical energy dissipation by plotting the maximum (taken at every point in time over the whole domain, i.e. not necessarily at the same location) of the electric energy density $\max[E^2]$, which should be conserved in ideal force-free MHD for a non-interacting wave.

We analyse the error in the electric energy density because the dissipation operator appears in Ampere's law (2.9). The electromagnetic energy at $N_{\lambda,z} = 8$ cells per wavelength has completely dissipated after 10 collisions and the error is equal to
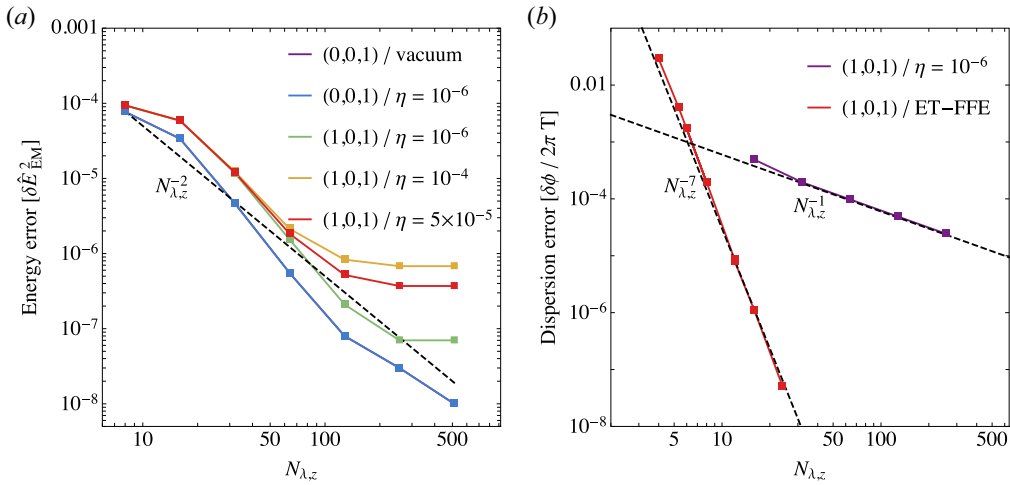
FIGURE 16. Convergence properties of the employed numerical methods. (*a*) Second-order convergence of the electric energy density error $\delta \hat{E}_{\text{EM}}^2 = || \max[\hat{E}_{\text{EM}}^2]_{\omega_0 t/2\pi=10} - \max[\hat{E}_{\text{EM}}^2]_{\omega_0 t/2\pi=0}||$ versus resolution per wavelength $N_{\lambda,z}$, for single waves with $\boldsymbol{k} = (0, 0, 1)$ in force-free MHD with $\eta = 10^{-6}$ (the force-free limit) and the electrovacuum limit, and for a single wave with $\boldsymbol{k} = (1, 0, 1)$ with $\eta = 10^{-6}$. For the $\boldsymbol{k} = (1, 0, 1)$ wave, we find that the explicit resistivity dominates the dissipation from $N_{\lambda,z} = 256$ onward, and the error saturates. For the $\boldsymbol{k} = (0, 0, 1)$ wave, we find that the error in the energy conservation is independent of the effective resistivity η as expected for a wave that has zero conduction current. We find second-order convergence, as expected for our IMEX scheme, both in the ideal force-free MHD limit $\eta \to 0$ and in the electrovacuum limit $\eta \to \infty$ in (2.11). For $N_{\lambda,z} = 8$ cells per wavelength, the error is equal to the initial wave energy because most energy is dissipated after 10 collisions. We confirm that the error is dominated by the spatial resolution and that it does not decrease for a decreasing time step at a given resolution of $N_{\lambda,z} = 16$. (*b*) The dispersion error of a single wave as the phase shift $\delta\phi = \delta x/2\pi$ of the nulls of the wave normalized by the number of wave periods $T = t/2\pi$. The error converges as first-order $N_{\lambda,z}^{-1}$ with grid points per wavelength and is dominated by the temporal error that is first order owing to the implicit step in the IMEX scheme for BHAC, whereas it converges at seventh order for the ET-FFE code.

the initial energy in the wave. By increasing the resolution per wavelength, we find second-order convergence of the error $\delta E^2 = || \max[E^2]_{\omega_0 t/2\pi=10} - \max[E^2]_{\omega_0 t/2\pi=0}||$ after ten wave-crossings, both in the ideal force-free MHD limit ($\eta \to 0$ in (2.11)), by setting $\eta = 10^{-7}$, and in the electrovacuum limit ($\eta \to \infty$ in (2.11)), by setting $\eta = 10^{14}$ (see figure 16). We confirm that the error in the energy conservation is independent of the effective resistivity for $\eta \in [10^{-3}, 10^{-4}, 10^{-5}, 10^{-6}, 10^{-7}]$. The specific resistivity sets a resistive spatial scale that cuts off the energy error convergence once it reaches that scale, thus, the error becomes smaller for smaller resistivity. We compare the result with a wave vector $\boldsymbol{k} = (0, 0, 1)$ that is aligned with the guide field, such that there is no damping term in (2.11) and hence the resistivity has no effect on the energy dissipation. There, we observe that the energy error converges at second order and there is indeed no cut-off at the resistive scale. The convergence is dominated by the spatial order of the scheme, which we validate by measuring the error for a decreasing time step at a fixed resolution of $N_{\lambda,z} = 16$. A similar analysis was conducted for the ET-FFE algorithm (Mahlmann *et al.* 2021*a*), showing convergence close to the spatial order of reconstruction, i.e. seventh-order in the simulations presented throughout this manuscript.
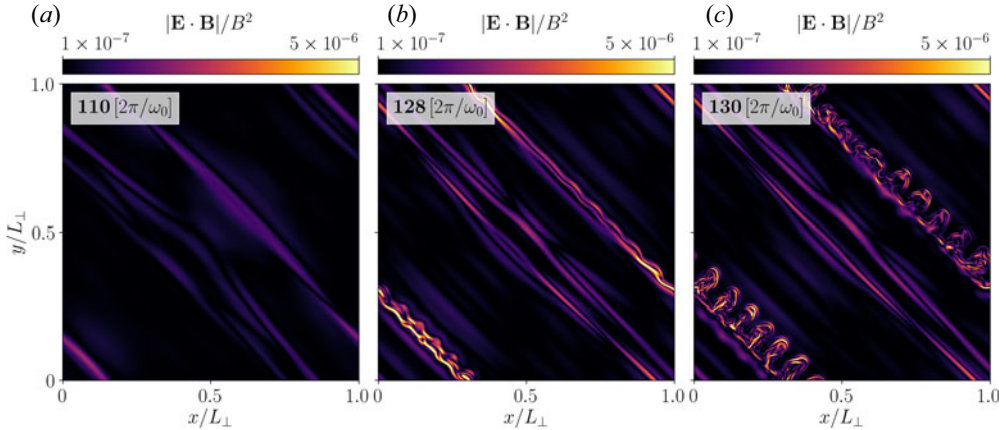
FIGURE 17. Non-ideal electric field $|\boldsymbol{E} \cdot \boldsymbol{B}|/B^2$ growing inside the current sheets. We examine such fields shortly after the formation of the sheets at $t = 110 \ [2\pi/\omega_0]$, at the end of the thinning period of the sheets to $\delta/w \approx 0.01$ at $t = 128 \ [2\pi/\omega_0]$ and at their break-up around $t = 130 \ [2\pi/\omega_0]$. Here, we employ the force-free MHD infrastructure in BHAC with $\eta = 10^{-6}$. The violations of the ideal force-free condition are damped by resistive dissipation (see § 2).

Furthermore, we determine the dispersion error as the shift $\delta\phi = \delta x/2\pi$ of the nulls of the wave normalized by the number of wave periods $T = t/2\pi$. We measure the error after 1, 10 and 20 wave-crossings and summarize the results in figure 16(*b*). The dispersion error is dominated by temporal errors and converges at first order owing to the implicit step that makes the IMEX scheme first order in time (Ripperda *et al.* 2019*a*). We confirm that the dispersion error linearly increases in time such that we can normalize the results by the wave period. With a seventh-order spatial reconstruction and fourth-order time integration, the dispersion error of the ET-FFE algorithm decreases slightly faster than the order of reconstruction. In other words, this method is more diffusive then it is dispersive and hence well suited for the long time modelling of wave interactions.

Appendix B. Non-ideal electric fields in (force-free) current sheets

Current sheets, i.e. regions of anti-parallel magnetic field where typically $\boldsymbol{E} \cdot \boldsymbol{B} \neq 0$ or $E^2 > B^2$, are inherently difficult to model in the force-free limit of infinite conductivity. Non-ideal electric fields, characterized by $\boldsymbol{E} \cdot \boldsymbol{B} \neq 0$, can form as a result of magnetic reconnection in a current sheet. Force-free evolution codes either allow for transient non-ideal electric fields and gradually dampen them (as is the case in BHAC, cf. (2.11)) or they remove them instantly from the domain in each sub-step of the time integrator (as it is the case in ET-FFE).

Figures 17 and 18 show the non-ideal electric fields accumulating in the different frameworks. In the case of the ET-FFE data, a direct measurement of $E_\parallel$ (or equally, of an Ohmic heating term) is not possible, as all violations of the force-free conditions are instantly removed from the domain. Instead, we track the magnitude of parallel electric fields that are algebraically removed in each sub-step of the time integrator, namely $\boldsymbol{E} \cdot \boldsymbol{B}/B^2$. In both cases, we find direct coincidence of the location of field reversals and other markers for current sheets with regions of stronger $E_\parallel$. Furthermore, such fields are still small at $t = 110 \ [2\pi/\omega_0]$, but they grow significantly during the thinning and break-up phases of the sheets.
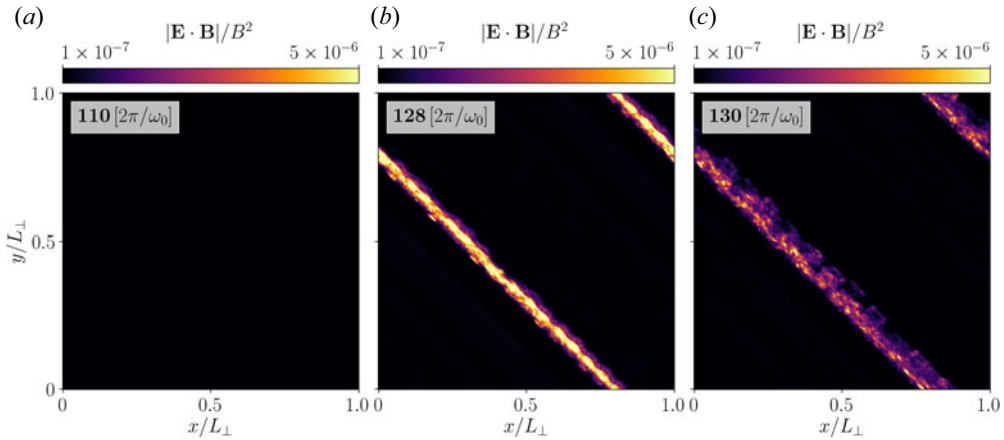
FIGURE 18. As in figure 17 but displaying the magnitude of the non-ideal electric field (averaged along the z-directions) that is removed in each sub-step of the time integrator at a given time by the ET-FFE scheme. We note the similarities to the non-ideal electric field that is allowed for finite times by BHAC (figure 17).

BHAC and ET-FFE differ significantly in their treatment of non-ideal electric fields. This distinction is imprinted on the data by the emergence of small-scale structures that are visible in figures 17 and 18. The combination of a finite phenomenological resistivity and lower-order spatial reconstruction in BHAC renders strong $E_\parallel$ significant for the resolution of thin resistive layers occurring in current sheets. ET-FFE deals with force-free violations much more rigorously, removing even the smallest $E_\parallel$ instantly and preventing the physical development of the smallest resistive layers (but increasing the overall order of convergence; see extensive discussion in Mahlmann *et al.* 2021*b*). The fact that despite these differences, our results across the platforms BHAC and ET-FFE show a remarkable level of similarity reassures us of the physical validity of the conclusions presented in this manuscript.

REFERENCES

ALIC, D., MOESTA, P., REZZOLLA, L., ZANOTTI, O. & JARAMILLO, J.L. 2012 Accurate simulations of binary black hole mergers in force-free electrodynamics. *Astrophys. J.* **754** (1), 36.

BHATTACHARJEE, A., HUANG, Y.-M., YANG, H. & ROGERS, B. 2009 Fast reconnection in high-Lundquist-number plasmas due to the plasmoid instability. *Phys. Plasmas* **16** (11), 112102.

BHATTACHARJEE, A. & NG, C.S. 2001 Random scattering and anisotropic turbulence of shear alfvén wave packets. *Astrophys. J.* **548** (1), 318–322.

BISKAMP, D. 2000 *Magnetic Reconnection in Plasmas*, vol. 3. Cambridge University Press.

BLANDFORD, R.D. 2002 To the lighthouse. In *Lighthouses of the Universe: The Most Luminous Celestial Objects and their Use for Cosmology* (ed. M. Gilfanov, R. Sunyaev & E. Churazov), p. 381. Springer.

BLANDFORD, R.D. & ZNAJEK, R.L. 1977 Electromagnetic extraction of energy from Kerr black holes. *Mon. Not. R. Astron. Soc.* **179**, 433–456.

BOLDYREV, S. 2005 On the spectrum of magnetohydrodynamic turbulence. *Astrophys. J. Lett.* **626** (1), L37–L40.

BOLDYREV, S. 2006 Spectrum of magnetohydrodynamic turbulence. *Phys. Rev. Lett.* **96** (11), 115002.

BRANSGROVE, A., BELOBORODOV, A.M. & LEVIN, Y. 2020 A quake quenching the vela pulsar. *Astrophys. J.* **897** (2), 173.

BURGERS, J.M. 1948 A mathematical model illustrating the theory of turbulence. *Adv. Appl. Mech.* **1**, 171–199. Elsevier.

ČADA, M. & TORRILHON, M. 2009 Compact third-order limiter functions for finite volume methods. *J. Comput. Phys.* **228**, 4118.

CHANDRAN, B.D.G. 2005 Weak compressible magnetohydrodynamic turbulence in the solar corona. *Phys. Rev. Lett.* **95**, 265004.

CHANDRAN, B.D.G., FOUCART, F. & TCHEKHOVSKOY, A. 2018 Heating of accretion-disk coronae and jets by general relativistic magnetohydrodynamic turbulence. *J. Plasma Phys.* **84** (3), 905840310.

CHANDRAN, B.D.G., SCHEKOCHIHIN, A.A. & MALLET, A. 2015 Intermittency and alignment in strong RMHD turbulence. *Astrophys. J.* **807** (1), 39.

CHERNOGLAZOV, A., RIPPERDA, B. & PHILIPPOV, A. 2021 Dynamic alignment and plasmoid formation in relativistic magnetohydrodynamic turbulence. *Astrophys. J. Lett.* (submitted).

CHO, J. 2005 Simulations of relativistic force-free magnetohydrodynamic turbulence. *Astrophys. J.* **621** (1), 324–327.

CHO, J. & LAZARIAN, A. 2002 Compressible sub-alfvenic MHD turbulence in low-β plasmas. *Phys. Rev. Lett.* **88** (24), 245001.

CHO, J. & LAZARIAN, A. 2003 Compressible magnetohydrodynamic turbulence: mode coupling, scaling relations, anisotropy, viscosity-damped regime and astrophysical implications. *Mon. Not. R. Astron. Soc.* **345**, 325–339.

CHO, J. & VISHNIAC, E.T. 2000 The anisotropy of magnetohydrodynamic alfvénic turbulence. *Astrophys. J.* **539** (1), 273–282.

COMISSO, L., HUANG, Y.M., LINGAM, M., HIRVIJOKI, E. & BHATTACHARJEE, A. 2018 Magnetohydrodynamic turbulence in the plasmoid-mediated regime. *Astrophys. J.* **854** (2), 103.

COMISSO, L. & SIRONI, L. 2018 Particle acceleration in relativistic plasma turbulence. *Phys. Rev. Lett.* **121** (25), 255101.

DEL ZANNA, L., PAPINI, E., LANDI, S., BUGLI, M. & BUCCIANTINI, N. 2016 Fast reconnection in relativistic plasmas: the magnetohydrodynamics tearing instability revisited. *Mon. Not. R. Astron. Soc.* **460** (4), 3753–3765.

DONG, C., WANG, L., HUANG, Y., COMISSO, L. & BHATTACHARJEE, A. 2018 Role of the plasmoid instability in magnetohydrodynamic turbulence. *Phys. Rev. Lett.* **121** (16), 165101.

DUNCAN, R.C. & THOMPSON, C. 1992 Formation of very strongly magnetized neutron stars: implications for gamma-ray bursts. *Astrophys. J. Lett.* **392**, L9.

EVANS, C.R. & HAWLEY, J.F. 1988 Simulation of magnetohydrodynamic flows: a constrained transport model. *Astrophys. J.* **332**, 659.

FARGE, M. & SCHNEIDER, K. 2006 *Encyclopedia of Mathematical Physics*. Elsevier.

GALTIER, S., NAZARENKO, S.V., NEWELL, A.C. & POUQUET, A. 2000 A weak turbulence theory for incompressible magnetohydrodynamics. *J. Plasma Phys.* **63** (5), 447–488.

GOLDREICH, P. & JULIAN, W.H. 1969 Pulsar electrodynamics. *Astrophys. J.* **157**, 869.

GOLDREICH, P. & SRIDHAR, S. 1995 Toward a theory of interstellar turbulence. II. Strong alfvenic turbulence. *Astrophys. J.* **438**, 763.

GRUZINOV, A. 1999 Stability in force-free electrodynamics. arXiv:astro-ph/9902288.

HEYL, J.S. & HERNQUIST, L. 1999 Nonlinear QED effects in strong-field magnetohydrodynamics. *Phys. Rev. D* **59** (4), 045005.

HOWES, G.G. 2014 The inherently three-dimensional nature of magnetized plasma turbulence. *J. Plasma Phys.* **81** (2), 325810203.

HOWES, G.G. 2016 The dynamical generation of current sheets in astrophysical plasma turbulence. *Astrophys. J.* **827** (2), L28.

HOWES, G.G., MCCUBBIN, A.J. & KLEIN, K.G. 2018 Spatially localized particle energization by Landau damping in current sheets produced by strong alfvén wave collisions. *J. Plasma Phys.* **84**, 905840105.

HOWES, G.G. & NIELSON, K.D. 2013 Alfvén wave collisions, the fundamental building block of plasma turbulence. I. Asymptotic solution. *Phys. Plasmas* **20** (7), 072302.

HUANG, Y.M. & BHATTACHARJEE, A. 2016 Turbulent magnetohydrodynamic reconnection mediated by the plasmoid instability. *Astrophys. J.* **818** (1), 20.

KOMISSAROV, S.S., BARKOV, M. & LYUTIKOV, M. 2007 Tearing instability in relativistic magnetically dominated plasmas. *Mon. Not. R. Astron. Soc.* **374** (2), 415–426.

KUZNETSOV, E.A. 2001 Weak magnetohydrodynamic turbulence of a magnetized plasma. *J. Expl Theor. Phys.* **93** (5), 1052–1064.

LI, X. & BELOBORODOV, A.M. 2015 Plastic damping of alfvén waves in magnetar flares and delayed afterglow emission. *Astrophys. J.* **815** (1), 25.

LI, X., BELOBORODOV, A.M. & SIRONI, L. 2021 Fast dissipation of colliding alfvén waves in a magnetically dominated plasma. arXiv:2103.05700.

LI, X., ZRAKE, J. & BELOBORODOV, A.M. 2019 Dissipation of alfvén waves in relativistic magnetospheres of magnetars. *Astrophys. J.* **881** (1), 13.

LONDRILLO, P. & DEL ZANNA, L. 2004 On the divergence-free condition in Godunov-type schemes for ideal magnetohydrodynamics: the upwind constrained transport method. *J. Comput. Phys.* **195** (1), 17–48.

LOUREIRO, N.F. & BOLDYREV, S. 2017 Role of magnetic reconnection in magnetohydrodynamic turbulence. *Phys. Rev. Lett.* **118** (24), 245101.

MAHLMANN, J.F. 2020 Dynamics in the magnetospheres of compact objects. PhD thesis, Universitat de València.

MAHLMANN, J.F., ALOY, M.A., MEWES, V. & CERDÁ-DURÁN, P. 2021*a* Computational general relativistic force-free electrodynamics. I. Multi-coordinate implementation and testing. *Astron. Astrophys.* **647**, A57.

MAHLMANN, J.F., ALOY, M.A., MEWES, V. & CERDÁ-DURÁN, P. 2021*b* Computational general relativistic force-free electrodynamics. II. Characterization of numerical diffusivity. *Astron. Astrophys.* **647**, A58.

MALLET, A., SCHEKOCHIHIN, A.A. & CHANDRAN, B.D.G. 2015 Refined critical balance in strong Alfvénic turbulence. *Mon. Not. R. Astron. Soc.* **449**, L77–L81.

MALLET, A., SCHEKOCHIHIN, A.A. & CHANDRAN, B.D.G. 2017 Disruption of Alfvénic turbulence by magnetic reconnection in a collisionless plasma. *J. Plasma Phys.* **83** (6), 905830609.

MARON, J. & GOLDREICH, P. 2001 Simulations of incompressible magnetohydrodynamic turbulence. *Astrophys. J.* **554**, 1175–1196.

MATTHAEUS, W.H. & LAMKIN, S.L. 1986 Turbulent magnetic reconnection. *Phys. Fluids* **29**, 2513–2534.

MEDIA SUPPLEMENT A 2021 Interaction of continuously overlapping alfvén waves: 2d current and field structure. https://youtu.be/HHacblwqiS0. The supplementary material was published on behalf of the authors of this manuscript.

MEDIA SUPPLEMENT B 2021 Interaction of continuously overlapping alfvén waves: 3d current structure. https://youtu.be/GTLvtH7CKOs. The supplementary material was published on behalf of the authors of this manuscript.

MEDIA SUPPLEMENT C 2021 Interaction of alfvén wave packets: 2d growth and dynamics of the $(1, 1)$ mode. https://youtu.be/Rd9qTNyaN5s. The supplementary material was published on behalf of the authors of this manuscript.

MEDIA SUPPLEMENT D 2021 Interaction of alfvén wave packets: 2d current and field structure for the $AW_3 + AW_3$ setup. https://youtu.be/E3wjj4blpg8. The supplementary material was published on behalf of the authors of this manuscript.

MEDIA SUPPLEMENT E 2021 Interaction of alfvén wave packets: 2d current and field structure for the $AW_1 + AW_3$ setup. https://youtu.be/iEIlV3q1Oto, The supplementary material was published on behalf of the authors of this manuscript.

MEDIA SUPPLEMENT F 2021 Interaction of alfvén wave packets: 3d current structure for the $AW_3 + AW_3$ setup. https://youtu.be/EMBVLRTtaHg. The supplementary material was published on behalf of the authors of this manuscript.

MEDIA SUPPLEMENT G 2021 Interaction of alfvén wave packets: 3d current structure for the $AW_1 + AW_3$ setup. https://youtu.be/Kdmz6ebLPiQ. The supplementary material was published on behalf of the authors of this manuscript.

MEDIA SUPPLEMENT H 2021 Interaction of alfvén wave packets: 3d growth and dynamics of the $(1, 1)$ mode. https://youtu.be/5RLFXu0D1Ps. The supplementary material was published on behalf of the authors of this manuscript.

MEYRAND, R., GALTIER, S. & KIYANI, K.H. 2016 Direct evidence of the transition from weak to strong magnetohydrodynamic turbulence. *Phys. Rev. Lett.* **116** (10), 105002.

MONIN, A.S. & YAGLOM, A.M. 1999 Statistical fluid mechanics: the mechanics of turbulence. https://mitpress.mit.edu/books/statistical-fluid-mechanics-volume-1.

MONTGOMERY, D. & MATTHAEUS, W.H. 1995 Anisotropic modal energy transfer in interstellar turbulence. *Astrophys. J.* **447**, 706.

NATHANAIL, A., FROMM, C.M, PORTH, O., OLIVARES, H., YOUNSI, Z., MIZUNO, Y. & REZZOLLA, L. 2020 Plasmoid formation in global GRMHD simulations and AGN flares. *Mon. Not. R. Astron. Soc.* **495** (2), 1549–1565.

NÄTTILÄ, J. & BELOBORODOV, A.M. 2020 Radiative turbulent flares in magnetically-dominated plasmas. arXiv:2012.03043.

NG, C.S. & BHATTACHARJEE, A. 1996 Interaction of shear-alfven wave packets: implication for weak magnetohydrodynamic turbulence in astrophysical plasmas. *Astrophys. J.* **465**, 845.

NG, C.S. & BHATTACHARJEE, A. 1997 Scaling of anisotropic spectra due to the weak interaction of shear-Alfvén wave packets. *Phys. Plasmas* **4** (3), 605–610.

NIELSON, K.D., HOWES, G.G. & DORLAND, W. 2013 Alfvén wave collisions, the fundamental building block of plasma turbulence. II. Numerical solution. *Phys. Plasmas* **20** (7), 072303.

NI, L., GERMASCHEWSKI, K., HUANG, Y.M., SULLIVAN, B.P., YANG, H. & BHATTACHARJEE, A. 2010 Linear plasmoid instability of thin current sheets with shear flow. *Phys. Plasmas* **17** (5), 052109.

NOBLE, S.C., GAMMIE, C.F., MCKINNEY, J.C. & DEL ZANNA, L. 2006 Primitive variable solvers for conservative general relativistic magnetohydrodynamics. *Astrophys. J.* **641** (1), 626–637.

OLIVARES, H., PORTH, O., DAVELAAR, J., MOST, E.R., FROMM, C.M., MIZUNO, Y., YOUNSI, Z. & REZZOLLA, L. 2019 Constrained transport and adaptive mesh refinement in the black hole accretion code. *Astron. Astrophys.* **629**, A61.

PARESCHI, L. & RUSSO, G. 2005 Implicit–explicit Runge–Kutta schemes and applications to hyperbolic systems with relaxation. *J. Sci. Comput.* **25** (1), 129–155.

PEREZ, J.C. & BOLDYREV, S. 2008 On weak and strong magnetohydrodynamic turbulence. *Astrophys. J. Lett.* **672** (1), L61.

PORTH, O., OLIVARES, H., MIZUNO, Y., YOUNSI, Z., REZZOLLA, L., MOSCIBRODZKA, M., FALCKE, H. & KRAMER, M. 2017 The black hole accretion code. *Comput. Astrophys. Cosmol.* **4**, 1.

RIPPERDA, B., BACCHINI, F. & PHILIPPOV, A.A. 2020 Magnetic reconnection and hot spot formation in black hole accretion disks. *Astrophys. J.* **900** (2), 100.

RIPPERDA, B., BACCHINI, F., PORTH, O., MOST, E.R., OLIVARES, H., NATHANAIL, A., REZZOLLA, L., TEUNISSEN, J. & KEPPENS, R. 2019*a* General-relativistic resistive magnetohydrodynamics with robust primitive-variable recovery for accretion disk simulations. *Astrophys. J. Suppl.* **244** (1), 10.

RIPPERDA, B., BACCHINI, F., TEUNISSEN, J., XIA, C., PORTH, O., SIRONI, L., LAPENTA, G. & KEPPENS, R. 2018 A comprehensive comparison of relativistic particle integrators. *Astrophys. J. Suppl.* **235** (1), 21.

RIPPERDA, B., PORTH, O., SIRONI, L. & KEPPENS, R. 2019*b* Relativistic resistive magnetohydrodynamic reconnection and plasmoid formation in merging flux tubes. *Mon. Not. R. Astron. Soc.* **485** (1), 299–314.

RIPPERDA, B., PORTH, O., XIA, C. & KEPPENS, R. 2017*a* Reconnection and particle acceleration in interacting flux ropes II. 3d effects on test particles in magnetically dominated plasmas. *Mon. Not. R. Astron. Soc.* **471** (3), 3465–3482.

RIPPERDA, B., PORTH, O., XIA, C. & KEPPENS, R. 2017*b* Reconnection and particle acceleration in interacting flux ropes I. Magnetohydrodynamics and test particles in 2.5d. *Mon. Not. R. Astron. Soc.* 3279–3298.

RUEDA, J.A.A., VERSCHAREN, D., WICKS, R.T., OWEN, C.J., NICOLAOU, G., WALSH, A.P., ZOUGANELIS, I., GERMASCHEWSKI, K. & VARGAS DOMÍNGUEZ, S. 2021 Three-dimensional magnetic reconnection in particle-in-cell simulations of anisotropic plasma turbulence. arXiv:2103.13232.

RUSANOV, V.V. 1961 Calculation of interaction of non–steady shock waves with obstacles. *J. Comput. Math. Phys. USSR* **1**, 267–279.

SCHEKOCHIHIN, A.A., NAZARENKO, S.V. & YOUSEF, T.A. 2012 Weak Alfvén-wave turbulence revisited. *Phys. Rev.* E **85** (3), 036406.

SONNERUP, B.U.O. & CAHILL, L.J.JR. 1967 Magnetopause structure and attitude from explorer 12 observations. *J. Geophys. Res.* **72**, 171.

SRIDHAR, S. & GOLDREICH, P. 1994 Toward a theory of interstellar turbulence. I. Weak alfvenic turbulence. *Astrophys. J.* **432**, 612.

SURESH, A. & HUYNH, H.T. 1997 Accurate monotonicity-preserving schemes with Runge–Kutta time stepping. *J. Comput. Phys.* **136** (1), 83–99.

TAKAMOTO, M. & LAZARIAN, A. 2017 Strong coupling of alfvén and fast modes in compressible relativistic magnetohydrodynamic turbulence in magnetically dominated plasmas. *Mon. Not. R. Astron. Soc.* **472** (4), 4542–4550.

TENBARGE, J.M. & HOWES, G.G. 2013 Current sheets and collisionless damping in kinetic plasma turbulence. *Astrophys. J.* **771** (2), L27.

TENBARGE, J.M., RIPPERDA, B., CHERNOGLAZOV, A., BHATTACHARJEE, A., MAHLMANN, J.F., MOST, E.R., JUNO, J., YUAN, Y. & PHILIPPOV, A.A. 2021 Weak alfvénic turbulence in relativistic magnetically dominated plasmas I: asymptotic solutions. *J. Plasma Phys.* (submitted).

THOMPSON, C. & BLAES, O. 1998 Magnetohydrodynamics in the extreme relativistic limit. *Phys. Rev.* D **57**, 3219–3234.

TROISCHT, P. & THOMPSON, C. 2004 Force-free magnetohydrodynamic waves: nonlinear interactions and effects of strong gravity. *Phys. Rev.* D **70** (12), 124030.

UZDENSKY, D.A., LOUREIRO, N.F. & SCHEKOCHIHIN, A.A. 2010 Fast magnetic reconnection in the plasmoid-dominated regime. *Phys. Rev. Lett.* **105**, 23.

VERDINI, A. & GRAPPIN, R. 2012 Transition from weak to strong cascade in MHD turbulence. *Phys. Rev. Lett.* **109** (2), 025004.

VERNIERO, J.L. & HOWES, G.G. 2018 The alfvénic nature of energy transfer mediation in localized, strongly nonlinear alfvén wavepacket collisions. *J. Plasma Phys.* **84**, 905840109.

VERNIERO, J.L., HOWES, G.G. & KLEIN, K.G. 2018 Nonlinear energy transfer and current sheet development in localized alfvén wavepacket collisions in the strong turbulence limit. *J. Plasma Phys.* **84**, 905840103.

WERNER, G.R. & UZDENSKY, D.A. 2017 Nonthermal particle acceleration in 3d relativistic magnetic reconnection in pair plasma. *Astrophys. J.* **843** (2), L27.

YUAN, Y., BELOBORODOV, A.M., CHEN, A.Y. & LEVIN, Y. 2020*a* Plasmoid ejection by alfvén waves and the fast radio bursts from SGR 1935 + 2154. *Astrophys. J.* **900** (2), L21.

YUAN, Y., LEVIN, Y., BRANSGROVE, A. & PHILIPPOV, A.A. 2020*b* Alfvén wave mode conversion in pulsar magnetospheres. arXiv:2007.11504.

ZHDANKIN, V., UZDENSKY, D.A., PEREZ, J.C. & BOLDYREV, S. 2013 Statistical analysis of current sheets in three-dimensional magnetohydrodynamic turbulence. *Astrophys. J.* **771** (2), 124.

ZHDANKIN, V., UZDENSKY, D.A., WERNER, G.R & BEGELMAN, M.C. 2017 Numerical investigation of kinetic turbulence in relativistic pair plasmas I. Turbulence statistics. *Mon. Not. R. Astron. Soc.* **474** (2), 2514–2535.